LAWRENCE
LIVERMORE
NATIONAL
LABORATORY

LLNL-JRNL-872870

# Benchmarking Density Functional Theory Methods for Efficient Calculations of a Strongly Correlated Li1-x Ni1-y O2-Delta System

S. Zhang, L. Wan, W. Sun, E. Lomeli, S. Weitzner

March 7, 2025

ACS Applied Energy Materials

## Disclaimer

# Benchmarking Density Functional Theory Methods for Efficient Calculations of Strongly Correlated $Li_{1-x}Ni_{1-y}O_{2-\delta}$ System

Shenli Zhang,[*,†,‡] Wenyu Sun,[†,‡] Eder G. Lomeli,[†,¶] Wonseok Jeong ,[§] Stephen E. Weitzner,[†,‡] and Liwen F. Wan[*,†,‡]

†*Materials Science Division, Lawrence Livermore National Laboratory, Livermore, CA 94550, U.S.A*

‡*Laboratory for Energy Applications for the Future (LEAF), Lawrence Livermore National Laboratory, Livermore, CA 94550, U.S.A*

¶*Department of Materials Science and Engineering, Stanford University, Stanford, CA 94305, U.S.A*

§*National Institute of Standards and Technology, Gaithersburg, MD 20899, U.S.A*

E-mail: zhang52@llnl.gov; wan6@llnl.gov

**Abstract**

Transition metal oxides (TMOs), such as $LiNiO_2$, are promising candidates for energy storage and electronic devices due to their unique electronic properties, exceptional physical and chemical characteristics, and ability to adopt multiple oxidation states. However, accurately predicting their properties using mean-field density functional theory (DFT) is challenging due to the presence of strongly correlated $d$-electrons and the complex interplay between their structural, electronic, and magnetic responses. These challenges are further exacerbated by the need to model defects, surfaces, and

interfaces, which require computationally efficient, large-scale simulations. To address these issues, we carry out a benchmark study on the $Li_{1-x}NiO_2$ system, evaluating the performance of several popular functionals. Our findings demonstrate that combining SCAN functional relaxation with single-step HSE calculations provides a practical and scalable computational strategy. This approach balances accuracy and efficiency, enabling high-throughput simulations of strongly correlated TMOs as well as an improved predictive modeling capability of TMOs for practical applications.

## Keywords

density-functional theory; hybrid functional; transition metal oxides; lithium nickel oxides; lithium ion battery; lithiation voltage

# Introduction

Transition metal oxides (TMOs) exhibit a unique combination of electronic and physicochemical properties that make them highly attractive for energy-related applications, as their versatile oxidation states and spin configurations can be tailored to facilitate various chemical reactions, defect formations, and structural transformations. Their distinct electronic features, including spin-orbit coupling, strong electron-electron interactions, and coupling among magnetic states, further position them as promising candidates for novel electronic and quantum technologies. However, advancing TMOs to meet specific application requirements through laboratory experimentation alone is both time-consuming and challenging, highlighting the importance of computational approaches to guide the targeted regulation of oxidation and spin states for achieving desired reactivity, stability, and electronic or topological properties. Despite their potential, the strongly correlated *d*-electrons in open-shell TMOs pose significant challenges for modeling and simulations, as accurately capturing their behavior often requires high-level theoretical methods. Techniques such as Quantum Monte Carlo (QMC)[1–4] and dynamical mean-field theory (DMFT)[5,6] are considered gold standards

for resolving the electronic structure of strongly correlated TMOs, but their computational cost and lack of scalability limit their practicality for large-scale simulations. Yet, for many TMO-related energy applications, both accuracy and computational efficiency are essential. For example, in battery research, there is a growing emphasis on understanding the formation mechanisms and dynamic evolution of the cathode-electrolyte interphase (CEI) to enable the rational design of durable and functional CEI for enhanced high-energy density cell performance. During electrolyte decomposition and CEI formation, precise characterization of charge transfer processes at TMO surfaces and accurate prediction of associated energetics are essential.[7] Additionally, large-scale interface models that incorporate realistic microenvironments—such as cation ordering, defect formation, surface contamination, surface reconstruction, electrolyte screening, and solvent/salt adsorption—are crucial for qualitatively elucidating key degradation mechanisms at the interfaces that drive CEI formation.[8–10] In solid oxide fuel cells, estimating charge carrier concentrations (such as protons, electrons, and holes) that control energy conversion efficiency relies on accurately calculating defect formation energies in both idealized single-crystal lattice representations[11] and polycrystalline structures that encompass possible grain boundaries and mixed phases.[12] This requires efficient computational approaches capable of handling hundreds of atoms while maintaining predictive fidelity. For applications such as solar water splitting, accurately predicting overall oxygen evolution kinetics on TMO surfaces necessitates theoretical models that scale up to resolve facet-dependent reaction pathways[13] and explicitly address the impact of the solvent environment.[14] To this end, density functional theory (DFT), a widely adopted mean-field approach, strikes a more practical balance between accuracy and computational efficiency, particularly when paired with a careful selection of exchange-correlation functionals, making it a more scalable and accessible option for studying TMOs in the above mentioned energy-related applications.

Although several benchmark studies have compared the accuracy of various DFT exchange-correlation energy functionals for TMOs,[6,15,16] and commonly adopted strategies for com-

bining models to predict properties have been developed (e.g., using single-step meta-GGA functionals on GGA-relaxed structures[17]), a fundamental understanding of the strengths and limitations of prevailing exchange-correlation energy functionals is still needed. Such understanding is crucial for guiding the selection of scalable exchange-correlation functionals capable of simultaneously addressing complex and diverse chemical environments.

DFT+U[18–21] and DFT+U+V[22,23] correction schemes have demonstrated effectiveness in predicting certain physicochemical properties of TMOs,[23–27] however, it remains virtually impossible to identify universal U, or U and V values for different oxidation states of a given element,[28] which usually occurs for transition metals during chemical reactions. Meta-GGA and hybrid DFT functionals present a potentially better alternative, as they provide a more refined description of the ground state electron density compared to semi-local functionals (*i.e.*, LDA and GGA) by incorporating the kinetic energy density and a portion of the exact exchange energy, respectively. However, previous studies shown U corrections may still be needed to achieve accurate electronic structure and energetics description of TMOs with SCAN.[16,29,30] With hybrid functionals, it also faces significant scalability challenges, particularly for simulations involving defects, surfaces, interfaces, or mixed phases, where realistic modeling often requires systems with more than hundreds of atoms to accurately represent local chemical environments.

To this end, in this work we develop a computational framework to enable rational functional selection and demonstrate its efficacy for improving the description of TMO cathode materials used in lithium-ion batteries (LIBs). Specifically, we consider $Li_{1-x}NiO_2$ as a test system, which is a particularly challenging yet promising TMO, widely studied as a potential high-energy-density cathode material for advanced LIBs. The primary challenges involve addressing two critical requirements: (1) accurately describing the Ni-3$d$/O-2$p$ hybridization, which governs the orbital filling of Ni and thus its electronic structures, the band gap of $LiNiO_2$, and the energy changes during lithiation/delithiation, thereby determining the voltage profile. This aspect depends on both onsite and intersite electron correlations, which are

highly sensitive to the choice of exchange-correlation functionals in DFT and the U and V parameters in DFT+U(+V) methods. (2) Correctly capturing the coupled local structure distortion-electronic-magnetic properties, as the open-shell nature of $Ni^{3+}$ in $LiNiO_2$ induces varying degrees of Jahn-Teller (JT) distortion and spin configurations, leading to multiple competing crystal structures, including $R\bar{3}m$ (no JT distortion), $C2/m$ (linear JT ordering), $P2_1/c$ (zig-zag JT ordering), and $P2/c$ ($Ni^{2+}/Ni^{4+}$ disproportionation). Numerous theoretical studies have sought to determine the relative stability of these phases, revealing significant sensitivity to the chosen exchange-correlation functional.[31–35]

Here, we use both experimental data and reference-level electronic structure theories to benchmark DFT functionals. Benchmarking the properties of the $Li_{1-x}NiO_2$ system purely against experimental data is difficult due to finite-temperature effects, statistical variations, and the potential presence of defects in the material. Most $LiNiO_2$ samples are off-stoichiometric, often containing excess Li, Ni-Li antisites, and oxygen vacancies. These factors significantly affect the material's ground-state structure, electronic properties, and overall physicochemical behavior. For instance, the $P2_1/c$ phase has been predicted as the ground-state structure using both PBE+U (with U = 5 eV) and HSE06.[31,34] However, this prediction contradicts experimental findings, which identify the $R\bar{3}m$ phase as the ground-state structure.[36] This discrepancy is likely influenced by temperature effects[37] and Li-Ni antisite disorder.[38,39] In this context, high-level electronic structure theories provide reliable references for benchmarking. Beyond DFT, $LiNiO_2$ has been studied using advanced theoretical methods, including Koopmans-compliant functionals,[40] many-body perturbation theory (GW),[41,42] DMFT,[43] and QMC.[4] QMC accurately predicts the energy variations of $Li_{1-x}NiO_2$ with changing Li content by correctly describing the Ni-3$d$/O-2$p$ hybridization. Certain methods, such as Koopmans-compliant functionals[40] and GW methods,[44] may exhibit specific limitations, including difficulty in accurately describing open-shell electronic configurations. Considering these limitations, QMC is chosen as the reference theory for benchmarking our $LiNiO_2$ calculations against existing literature results.

In this work, we evaluate the performance of various DFT functionals and correction methods for predicting the structure, electronic properties, and physicochemical characteristics of bulk $Li_{1-x}NiO_2$. We specifically compare the PBE, $r^2$SCAN, SCAN, and HSE06 functionals, alongside the PBE+U and PBE+U+V correction schemes. Our benchmarking evaluates three critical aspects of $Li_{1-x}NiO_2$ compositions, which are particularly sensitive to electronic and lattice structures: (1) the energy difference between the non-JT $R\bar{3}m$ phase and the JT-distorted $C2/m$ phase of $LiNiO_2$; (2) the energy variation in $Li_{1-x}NiO_2$ as a function of Li content ($x = 0, 0.25, 0.5, 0.75, 1.0$); and (3) the formation energies of common point defects, including Li vacancies, O vacancies, and Li-Ni antisites. We found that the HSE06 functional demonstrates superior accuracy in predicting the electronic, structural, and thermodynamic properties of $Li_{1-x}NiO_2$, as anticipated. The SCAN functional performs comparably well for local structure predictions, particularly in capturing the degree of JT distortion, which is critical for understanding the electronic response to local defect formation. The PBE+U and PBE+U+V methods, with carefully chosen U and V values, can yield energetics and electronic structures similar to HSE06. However, they struggle to accurately capture local JT distortions, and their results are highly sensitive to the specific U and V parameters. Based on these findings, we propose a practical workflow to balance computational accuracy and efficiency in modeling the $Li_{1-x}NiO_2$ system and relevant cathode materials with open-shell TMOs.

# Methods

The Vienna Ab initio Simulation Package (VASP) v5.4[45,46] was used to perform DFT calculations with the HSE06,[47] SCAN,[48] r$^2$SCAN,[49] PBE,[50,51] and PBE+U functionals. PBE+U calculations were carried out following the approach of Dudarev et al.[18] PAW-GGA pseudopotentials were employed with an energy cutoff of 520 eV, using valence configurations of Li: $2s^1$, Ni: $3p^6 3d^9 4s^1$, and O: $2s^2 2p^4$. For DFT+U+V calculations, the Quantum Espresso

(QE) software package v7.2[52–54] was utilized with the extended Hubbard functional[22] and SSSP pseudopotentials,[55] applying an energy cutoff of 680 eV. Semi-core states were explicitly included in the Li and Ni pseudopotentials, with valence configurations of Li: $1s^2 2s^1$ and Ni: $3s^2 3p^6 3d^8 4s^2$. The k-point mesh density for all DFT calculations was set to 0.06 $Å^{-1}$, with energy and force convergence thresholds of 0.2 meV and 10 meV/Å, respectively.

We note here that the choice of pseudopotentials can lead to quantitative differences in PBE+U(+V)-predicted properties, such as the voltage profile, local structural distortion, band gap, and magnetic states, as discussed in the Results section. However, we do not expect these discrepancies to qualitatively affect the predicted results. By comparing the calculated density of states (Fig. S14) using different pseudopotentials in QE (for PBE+U+V) and VASP (for all other functionals), we find that the differences caused by pseudopotentials are much smaller than those caused by different exchange-correlation functionals. Therefore, we believe the general conclusions drawn from this study remain unaffected by these technical details.

In this work, we considered the ferromagnetic (FM) ordering of $LiNiO_2$, which was shown to be the lowest magnetic state with PBE+U (U> 3 eV).[56] Additionally, for JT distorted structures, the energy difference between antiferromagnetic (AFM) and FM ordering is generally negligible (less than 1 meV/atom).[34]

For the PBE+U calculations, we tested several U values (4.5 eV, 6 eV, and 6.7 eV) to investigate how the predicted properties of $Li_{1-x}NiO_2$ vary with U. Additionally, we calculated the U and V values self-consistently for the $C2/m$ phase by updating lattice parameters at each cycle, using density-functional perturbation theory as implemented in the HP code in Quantum Espresso (QE).[57] We obtain U = 8.76 eV and V values of 0.72 eV and 0.55 eV for the short and long Ni-O bond lengths, respectively, due to JT distortion. Since the optimal U and V values are sensitive to local structures, symmetry, and the choice of pseudopotentials, this benchmark study does not aim to determine the exact optimal U and V for each structure but rather to understand the implications of such corrections. To

enable a systematic and consistent comparison across various $Li_{1-x}NiO_2$ structures and other DFT functionals, we adopted U = 6 eV and V values of 0.72 eV and 0.55 eV for this study.

Our benchmark study evaluates the accuracy of various DFT functionals and methods in predicting the structural and thermodynamic properties of the $R\bar{3}m$ and $C2/m$ structures of bulk $LiNiO_2$. The $R\bar{3}m$ phase exhibits rhombohedral symmetry and lacks JT distortion of the $NiO_6$ octahedra, consistent with experimental observations, and is represented using a hexagonal unit cell where Li and Ni alternate along the c-axis (see Fig. 1a). In contrast, the $C2/m$ phase adopts a monoclinic structure that accommodates JT distortion at each Ni site along the same symmetry zone axis (see Fig. 1a, where blue lines denote its primitive cell and black lines indicate the unit cell used in our calculations). Notably, the previously established ground-state structure of $LiNiO_2$ features a zig-zag JT distortion pattern with slightly reduced symmetry. For benchmarking and computational efficiency, we focus on the $C2/m$ phase with collinear JT distortion. The energy difference between the two monoclinic configurations is negligible (approximately 4 meV/atom at the PBE+U level of theory[34]), and both configurations exhibit nearly identical electronic properties.[34,58]

For the delithiated case, the initial structures of $Li_{1-x}NiO_2$ at $x$ = 0, 0.25, 0.5, 0.75, and 1 were adopted from a previous theoretical study, where various lithium arrangements were tested at the PBE level to identify the lowest-energy configurations consistent with experimental observations.[4] The resulting simulation supercells consist of 12 to 16 atoms, depending on the lithium content.

For point defects in bulk $LiNiO_2$, three common types of neutral defects are considered, *i.e.*, O vacancy, Li vacancy, and Li-Ni antisite. The cell dimensions are optimized using PBE+U (U = 6 eV), and the atomic positions are relaxed at different levels of theory. The defect formation energies are calculated using the following equations:

$$\mathrm{E_{Ovac}} = \mathrm{E} - \mathrm{E_0} + \frac{1}{2}\mathrm{E_{O_2}} \tag{1}$$

$$E_{Livac} = E - E_0 + E_{Li} \quad (2)$$

$$E_{Li\text{-}Ni} = E - E_0 \quad (3)$$

where $E_{Ovac}$, $E_{Livac}$, and $E_{Li-Ni}$ are the defect formation energies of O vacancy, Li vacancy, and Li-Ni antisite, respectively; E and $E_0$ are the total energies of supercells with and without defects; $E_{O_2}$ is the energy of the reference $O_2$ molecule in its triplet ground state, and $E_{Li}$ is the energy per Li atom in a body-centered cubic Li metal lattice. It is well known that the PBE functional can overestimate $E_{O_2}$. In this work, we apply a correction scheme proposed in Ref.,[59] using the experimental formation energy of $H_2O$ as a reference. Details of this correction are provided in the Supporting Information (SI) (Table S1). The optimized atomic coordinates for all of the SCAN-relaxed structures can be found at the end of the SI.

# Results and discussion

## Bulk properties of $LiNiO_2$ $R\bar{3}m$ and $C2/m$ phases

We begin our evaluation by comparing the predicted energy difference between the $R\bar{3}m$ and $C2/m$ phases ($\Delta E = E_{R\bar{3}m} - E_{C2/m}$, Fig. 1b) obtained using different DFT functionals and methods. Two simulation and benchmarking protocols were tested: (1) using fixed atomic positions and lattice dimensions for each phase (denoted as SCF in Fig. 1b, with lattice parameters provided in Table S3; the $R\bar{3}m$ structure was optimized at the PBE level, while the $C2/m$ structure was optimized using the SCAN functional); and (2) using fully optimized atomic structures at each level of theory. Comparing the results from these two procedures allows us to evaluate the influence of the predicted electronic structure on thermodynamic energies and the resulting lattice configurations. This comparison is particularly important for capturing local JT distortions and understanding their contribution to phase stability.

Using the first simulation protocol, where atomic positions and lattice structures are fixed, significant variations in the predicted $\Delta E$ are observed — up to 360 meV/f.u. between PBE

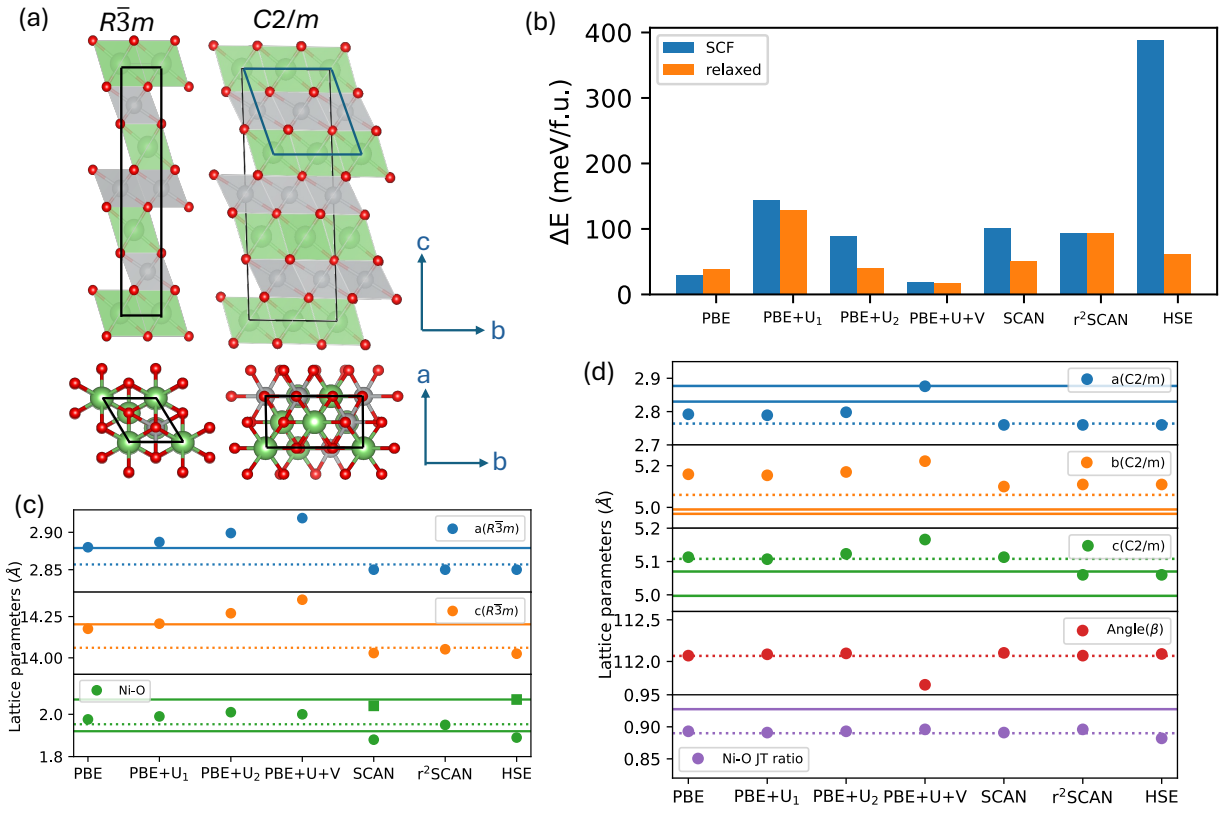


Figure 1: Comparison of energy and structural properties computed by different DFT methods. (a) Side view and top view of two possible crystal symmetries of $LiNiO_2$. Color scheme: Li: green; Ni: grey; O: red. (b) Computed energy difference $\Delta E = E_{R\bar{3}m} - E_{C2/m}$ for self-consistent calculation (denoted as SCF) and after structural optimization by each DFT method (denoted as relaxed). Lattice parameters (including angles) and Ni-O bond length of (c) $R\bar{3}m$ and (d) $C2/m$ phases predicted by various DFT methods. The solid lines represent literature reported experimental lattice parameters with X-ray diffraction [60,61] and Ni-O bond lengths with extended X-ray absorption fine structure (EXAFS) spectra, [62] where multiple values may present. We note in the $R\bar{3}m$, Ref. [62] assumes local JT distortion to occur when fitting EXAFS spectra and obtained two Ni-O bond length. Dotted line represent values before optimization. $U_1$=4.5 eV; $U_2$=6.7 eV; U+V: U=6 eV, V=0.55 and 0.72 eV.

and HSE06 (Fig. 1b) — across different DFT functionals and methods, highlighting the sensitivity of $\Delta E$ to onsite and intersite correlation energies. As shown in Fig. S1, $\Delta E$ generally decreases with increasing U, while exhibiting a non-monotonic dependence on changes in V. A correlation between predicted phase stability and the electronic structure of $LiNiO_2$, particularly in terms of the Ni oxidation states and the Ni-3$d$ and O-2$p$ orbital hybridization, was identified. As shown in Fig. 2, the Ni 3$d$-O 2$p$ orbital hybridization (the overlap between the Ni 3$d$-band center and the O 2$p$ center; see SI for a detailed explanation) progressively increases from PBE to r$^2$SCAN, SCAN, PBE+U(+V), and HSE06, which contributes to the observed increase in $\Delta E$ across these levels of theory (Fig. 1b). This trend can be rationalized by the fact that when the Ni oxidation state is closer to 3+, which has the $e_g^1 t_{2g}^6$ orbital configuration, the system favors a JT-distorted structure, thus leading to larger $\Delta E$. Notably, the increased covalency of the Ni-O bond and the O 2$p$ band center being higher than that of the Ni 3$d$ (observed only with PBE+U/V and HSE06) supports a negative charge-transfer picture,[63] i.e., the $3d^8\underline{L}^n$ configuration (where a finite density $n$ of holes $\underline{L}^n$ is self-doped into the O 2$p$ band). This observation aligns with recent experimental[62] and theoretical studies.[64,65]

The degree of $d$-$p$ hybridization and relative band alignment also correlates with the predicted magnetic moment of Ni, as shown in Fig. S3. While all functionals predict a magnetic moment of approximately 1 $\mu_B$/Ni for both phases, there is a slight increase in the predicted magnetic moment moving from PBE to $r^2$SCAN, SCAN, and HSE06 functionals, consistent with the trend observed in the predicted $\Delta E$ values. Notably, HSE06 predicts the Ni oxidation state to be closest to 3+. With PBE+U(V) corrections, we found that the predicted magnetic moment tends to increase with increasing U values. Specifically, at U= 6 eV and V=0.72 and 0.55 eV, the predicted magnetic moment of Ni exceeds the value predicted by the HSE06 functional, resulting in a lower oxidation state of Ni. This is likely due to an over-correction of the relative band alignment between Ni 3$d$ and O 2$p$, where the O 2$p$ energy level is predicted to be higher than that of Ni 3$d$. In contrast, moving from SCAN

to $r^2$SCAN and then to PBE functionals, the predicted oxidation state of Ni trends toward 4+ (characterized by lower $\Delta E$ and lower magnetic moment values, as shown in Figs.1b and S3). Given that the electronic structure of Ni is likely to be in the $3d^8\underline{L}^n$ configuration in $LiNiO_2$[62,64,65] as discussed, HSE06 and the PBE+U+V method, with appropriately chosen U and V values, are likely more accurate than SCAN-family functionals for describing the electronic structure of $LiNiO_2$. This conclusion aligns with a prior benchmark study that compared predicted charge density profiles from PBE, PBE+U, and SCAN functionals to DMC results.[4]

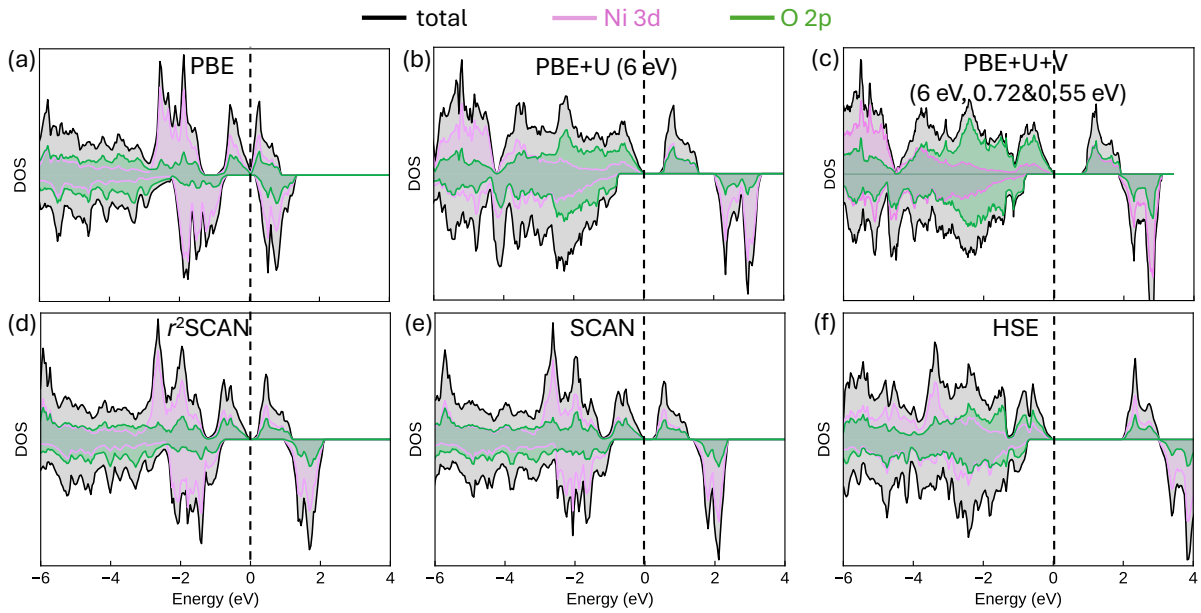


Figure 2: PDOS of the SCAN-relaxed $C2/m$ primitive cell computed from various functionals .(a)PBE; (b)PBE+U (U=6 eV); (c)PBE+U+V (U=6 eV, V=0.72 and 0.55 eV for short and long Ni-O bonds, respectively; (d)$r^2$SCAN; (e)SCAN; (f)HSE06.

Upon structural relaxation (Fig. 1b, where experimental values are indicated as colored solid lines), $\Delta E$ generally decreases compared to the fixed-structure case across most functionals, except for PBE. Among the tested functionals, HSE06, SCAN, and PBE+U (with U $\approx$ 6 eV) show the most significant variations (Fig. S4). These variations are positively correlated with changes in Ni-O bond lengths observed in the $R\bar{3}m$ phase during structural optimization. Notably, SCAN and HSE06 resolve spontaneous JT distortions even within

the hexagonal cell setting without initial symmetry breaking (see SI for detailed discussion). Both functionals predict local Ni-O bond lengths that align closely with experimental measurements, as illustrated in Fig. 1b. Interestingly, while PBE+U+V introduces the largest changes in predicted lattice parameters for both phases, the $\Delta E$ remains largely unaffected. This suggests that local structural distortions or changes in Ni-O bond lengths, rather than overall lattice dimensions, dominate the energy differences between the two phases. By separating the contributions of relative Ni-3$d$/O-2$p$ band alignment, JT distortion, and overall lattice structure to thermodynamic energies, we conclude that SCAN and HSE06 functionals are more effective at capturing JT distortion-induced local structural variations and are more sensitive to the coupling between electronic and lattice structures. In contrast, the PBE+U(+V) method fails to capture JT distortions without an initial symmetry break, which may lead to inaccuracies in predicting phase transitions and chemical reactivity. This highlights the importance of self-consistent determination of the electronic structure and the Ni-O local atomic environment.

To complete our evaluation of DFT functionals in predicting the electronic properties of $LiNiO_2$, we present the calculated band gap values of the $C2/m$ phase in Table1. For the $R\bar{3}m$ phase, all functionals predict a metallic state, as expected, since the degeneracy of the two half-filled $e_g$ orbitals is preserved in the absence of JT distortion. This result aligns with previous studies.[34] For the SCAN- and HSE06-relaxed structures, where specific JT distortion patterns are evident, the electronic structures remain metallic, likely due to varying degrees of degeneracy in the JT-distorted O-2$p$ orbitals, as also discussed by Chen *et al.*[34] In contrast, for the monoclinic phase, which inherently exhibits a JT distortion, the band gap predicted by PBE+U (with U=6 eV) is 0.26 eV, closely matching experimental reference values. Adding the V correction further increases the band gap. While the SCAN-family functionals generally underestimate the band gap, HSE06 tends to overestimate it. Adjusting the mixing parameter in HSE from 0.25 to 0.18 can recover the band gap to align with the G0W0@GGA+U predicted value, as shown in Ref.[41] However, accurate prediction

of the band gap is found to depend heavily on tuning fitting parameters, such as U and V in PBE+U or the mixing parameter in HSE. This dependence likely arises from the need for a faithful description of atomic structure and electronic interactions at both ground-state and excited-state levels, including self-interaction, onsite, and intersite Coulomb interactions. The imperfect match of tested methods and parameters highlights potential deficiencies in mean-field theory for capturing many-body effects. This work primarily focuses on establishing a computational protocol for capturing local structural distortion and associated energy changes due to defect formation and oxidation state changes of TM elements (e.g., during (de)lithiation). For scenarios requiring accurate band gap predictions, such as electronic conductivity, we recommend alternative correction schemes, including tuning the mixing parameter of the HSE functional or applying higher-level theories beyond DFT.

Table 1: **Band gaps**: Computed band gaps of $LiNiO_2$ by various DFT functionals and methods. Experimental reference[66] indicates a 0.4 eV band gap with photoemission.

| $E_g$ (eV) | PBE | PBE+U | PBE+U+V | r$^2$SCAN | SCAN | HSE06 |
|---|---|---|---|---|---|---|
| $C2/m$ phase | metallic | 0.26 | 0.8 | 0.1 | 0.17 | 2.13 |

U=6 eV and V=0.72 (longer Ni-O bond) and 0.55 (shorter Ni-O bond, or in the $R\bar{3}m$ phase).

## Impact of Li concentration in bulk $Li_{1-x}NiO_2$

Next, we compare the performance of DFT functionals in predicting the electronic and thermodynamic properties of $Li_{1-x}NiO_2$ as a function of lithium content, with relevance to its application as a high-voltage lithium intercalation cathode. In Fig.3, we present the calculated lithium intercalation voltage profile of $Li_{1-x}NiO_2$ at different levels of theory and compare the results with experimental data and previous theoretical studies. The intercalation voltage, $V$, is calculated as follows:

$$V \approx -\frac{E(\mathrm{Li_{x_1}NiO_2}) - E(\mathrm{Li_{x_2}NiO_2}) - (x_1 - x_2)E(\mathrm{Li})}{(x_1 - x_2)F} \tag{4}$$

where $x_1$ and $x_2$ represent the lithium concentrations, $F$ is the Faraday constant, and $E$ and $E_{\mathrm{Li}}$ are the total energies of fully relaxed $\mathrm{Li}_{1-x}\mathrm{NiO}_2$ and a lithium metal atom, respectively.

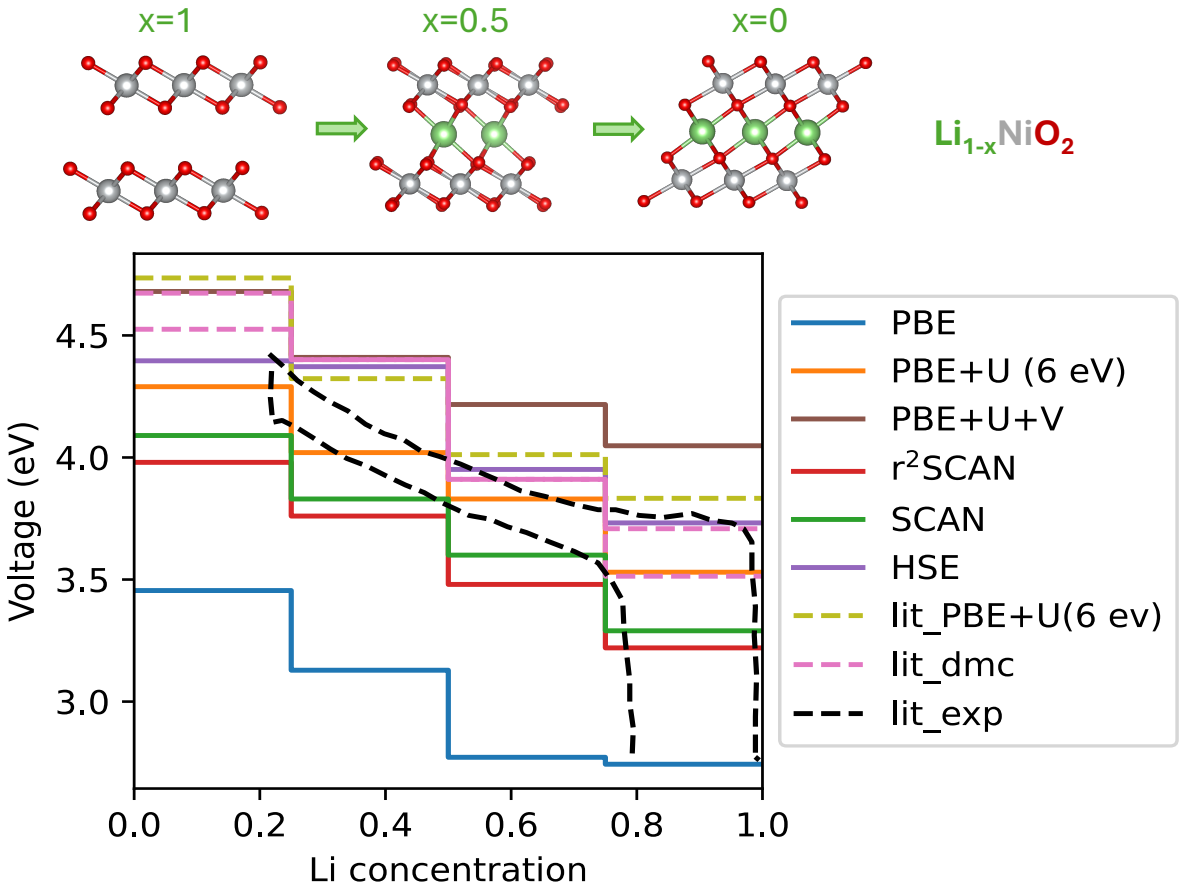


Figure 3: Calculated voltage change in $\mathrm{Li}_{1-x}\mathrm{NiO}_2$ as a function of Li concentration by various density functional methods. The corresponding crystal structures for x=0, 0.5 and 1 are shown on top of the figure. Experimental values (lit_exp) and profiles obtained by Diffusion Monte Carlo (lit_dmc) and PBE+U calculations [lit_PBE+U (6 eV)] in literatures[4,67] are included for comparison. Ni: grey; O: red; Li: green.

Overall, Fig.3 shows that the PBE+U (U = 6 eV) and HSE functionals most accurately reproduce the experimental data[67] and DMC reference values.[4] In contrast, the $r^2$SCAN and SCAN functionals appear to slightly underestimate the intercalation voltage. It is important to note that the accuracy of PBE+U predictions is highly sensitive to the choice of the U parameter and the pseudopotentials employed. For instance, Saritas et al. showed that the calculated Li intercalation voltage increases with increasing U values and that the predicted

voltage curve can shift upwards by 0.5 eV with a 3 eV increase in U and becomes flatter across the entire lithium intercalation window.[4] In this study, we also examined the impact of pseudopotentials on the voltage profile, as shown in Fig.S6. Since the U parameter is influenced by the choice of pseudopotentials, it is unsurprising to observe a ∼0.75 eV difference in the calculated voltage when using the same U value but different pseudopotentials. This sensitivity explains the discrepancies between our calculated voltage profile and literature values obtained at the same PBE+U level of theory. Additionally, incorporating a V correction systematically reduces the energy differences between $Li_{0.75}NiO_2$ and $Li_{0.5}NiO_2$, as well as between $LiNiO_2$ and $Li_{0.75}NiO_2$, resulting in a shallower voltage profile compared to PBE+U (Fig.S7). This effect may arise because the addition of V slightly decreases *p*-*d* hybridization (Fig.2), leading to a higher Ni oxidation state (see discussion in Section) and energetically favoring delithiation relative to PBE+U. In summary, the HSE functional and PBE+U (with an optimized U value, approximately 6 eV) provide the most accurate description of the energetics during the Li intercalation reaction. Similar to $LiNiO_2$ case, the energetics is tightly related to the electronic structure description of the phases, where we also found PBE+U leads to similar $d-p$ hybridization as in HSE06 calculations (Fig. S9).

Beyond energetics, it is crucial to highlight the importance of reliable structural predictability across different DFT functionals and methods. For instance, using the same PBE-relaxed structures for all functionals when calculating the Li intercalation voltage can lead to inaccurate energy profiles, particularly at Li concentrations between 0.75 and 1 when employing SCAN-family and HSE functionals (Fig. S8). This discrepancy arises primarily from the inadequate description of the JT distortion of $Ni^{3+}$, as illustrated in Fig. 1c and detailed in Tables S7 and S8. Since the JT distortion is a key factor in stabilizing the energetically favorable monoclinic phase of $LiNiO_2$, insufficient representation of this distortion reduces the energy gain associated with Ni transitioning from a 4+ to a 3+ oxidation state (see discussion in SI on the electronic structures of $Li_{1-x}NiO_2$ and Table S6 on how we determine the oxidation state of Ni). This, in turn, leads to incorrect predictions of the Li

intercalation voltage. Thus, accurately capturing the structural distortions, particularly the JT effect, is essential for achieving reliable voltage predictions.

## Point defects in bulk $LiNiO_2$: O vacancy, Li vacancy and Li-Ni antisite

It is well established that during the operation of $LiNiO_2$ as a Li intercalation cathode, various atomic defects can emerge. Here, we compare the performance of different DFT functionals in predicting the defect properties of bulk $LiNiO_2$ in the $C2/m$ phase. Three common types of neutral defects are considered, *i.e.*, O vacancy, Li vacancy, and Li-Ni antisite, as illustrated in Fig. 4. For the Li-Ni antisite defect, we tested two cases: swapping a nearest-neighbor Li-Ni pair and swapping a Li-Ni pair two cation layers apart (Figs. 4c and 4d). The computed defect formation energies using various DFT functionals are summarized in Table 2. Notably, PBE+U with a proper choice of $U$ can predict similar defect formation energies as the HSE06 functional for all tested cases, likely because the $U$ parameter was specifically fitted to the energies, as discussed previously. However, we highlight that the resulting defect formation energies can be highly sensitive to the $U$ value applied, as shown in Table S9. All functionals consistently predict the same ranking of defect formation energies, *i.e.*, $E_{Li-Ni} < E_{Ovac} < E_{Livac}$ and $E_{Li-Ni-case1} < E_{Li-Ni-case2}$, highlighting the general applicability of DFT in predicting the relative stability of different types of defects in $LiNiO_2$. Experimental observations further confirm these stability rankings. For example, the relatively low formation energy of the Li-Ni antisite defect is consistent with the common observation of Ni in the Li layers in as-synthesized $LiNiO_2$.[68–70] Oxygen vacancies have also been reported in as-synthesized $LiNiO_2$, but unlike the inevitable appearance of Li-Ni antisites, the concentration of oxygen vacancies is found to be highly dependent on the $O_2$ partial pressure and flow rate during synthesis.[62,71] This observation aligns with our predicted higher $E_{Ovac}$ compared to $E_{Li-Ni}$. Finally, Li vacancies typically appear during the delithiation (charging) process, which requires an external voltage, and thus are expected to

have higher formation energies. We conclude from Table 2 that the PBE+U method may predict defect formation energies as accurately as the HSE06 functional, likely due to the fact that the $U$ parameter is explicitly fitted to formation energies.[72] Without an empirical fitting parameter, the SCAN levels of theory tend to fall short in accurately predicting these defect formation energies, likely due to an inaccurate description of Ni-3$d$ and O-2$p$ hybridization in $LiNiO_2$, as discussed in Fig. 2.

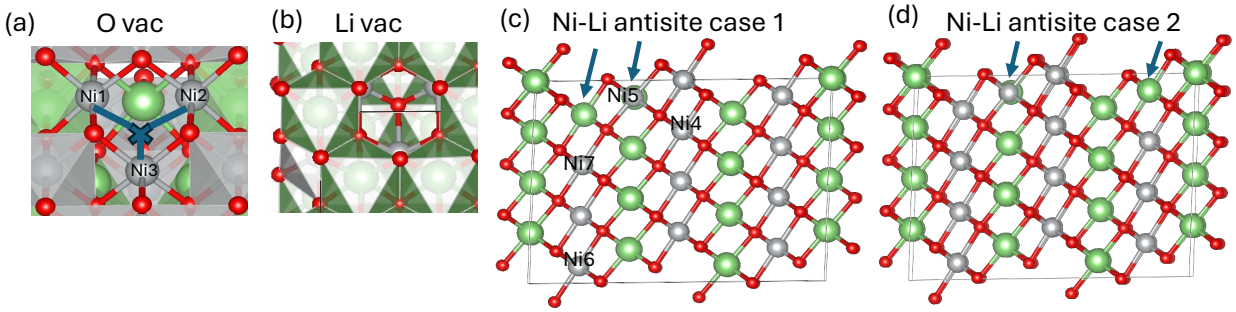


Figure 4: Defect atomic structures in $LiNiO_2$ bulk supercell used in this study: (a) oxygen vacancy, the missing Ni-O bonds for $Ni_1$ and $Ni_2$ sites are shorter than that of $Ni_3$ site due to existing JT distortion. (b) Li vacancy; (c) Li-Ni antisite configuration 1; (d) Li-Ni antisite configuration 2. Li: green; Ni: grey; O: red.

Table 2: **Defect formation energies**: Computed defect formation energies in bulk $C2/m$ $LiNiO_2$ by various DFT functionals and methods. U=6 eV, V=0.72 eV and 0.55 eV for long and short Ni-O bond lengths, respectively.

| Formation energy (eV) | PBE+U | PBE+U+V | r$^2$SCAN | SCAN | HSE06 |
|---|---|---|---|---|---|
| $E_{Ovac}$ | 1.66 | 1.77 | 2.61 | 2.66 | 1.34 |
| $E_{Livac}$ | 3.79 | 4.47 | 3.04 | 3.02 | 3.87 |
| $E_{Li-Ni-case1}$ | 0.91 | 1.14 | 0.38 | 0.32 | 0.82 |
| $E_{Li-Ni-case2}$ | 1.25 | 1.39 | 0.56 | 0.38 | 1.18 |

Introducing defects inevitably alters the electronic structure of $LiNiO_2$ due to local charge renormalization. Here, we examine the impact of defect formation on the electronic properties of $LiNiO_2$, with a particular focus on the redox behavior of Ni as predicted by different levels of theory. The oxidation state of Ni is determined based on its magnetic state (see Table S6 and related discussion in SI), while the degree of JT distortion, quantified by the ratio of shorter to longer Ni-O bond lengths, is also found to serve as an indicator of changes

in Ni oxidation state. Specifically, the JT distortion tends to decrease for both $Ni^{2+}$ and $Ni^{4+}$. Table 3 summarizes the Ni sites where charge transfer occurs — either from $Ni^{3+}$ to $Ni^{2+}$ or from $Ni^{3+}$ to $Ni^{4+}$ — as a result of defect formation, as predicted by various theoretical methods.

When introducing an O vacancy, the PBE+U+V, SCAN-family, and HSE06 functionals consistently resolve the expected change in oxidation state for two neighboring Ni atoms, from 3+ to 2+. In contrast, PBE+U predicts a more delocalized charge redistribution involving three neighboring Ni atoms, as shown in Fig.4a. For the Li vacancy case, only r$^2$SCAN, SCAN, and HSE06 functionals accurately capture the local charge transfer, where a single Ni atom adjacent to the vacancy site changes its oxidation state from 3+ to 4+. Both PBE+U and PBE+U+V, however, predict a uniform charge redistribution across all Ni atoms within the NiO6 layer. In the case of a Li-Ni antisite configuration, the Ni atom occupying the Li site reduces its neighboring Ni atoms (denoted as $Ni_{4,5,6}$ in Fig. 4c), while the Li atom at the Ni site promotes oxidation of nearby Ni atoms from 3+ to 4+. This charge renormalization behavior is captured by all DFT functionals, though PBE+U persistently predicts a more spatially delocalized charge transfer process. Across all defect calculations, no in-gap, defect-induced electronic states were observed for any of the DFT functionals. Visualization of the charge densities corresponding to energy states near the Fermi level (Fig. S10) further confirms the strong charge localization predicted by the HSE06 functional, followed by SCAN and r$^2$SCAN, which is attributed to the higher degree of JT distortion captured by these functionals compared to PBE and PBE+U(+V). We found that although the exact degree of charge renormalization, including both the spatial distribution and the number of Ni atoms switching oxidation states, varies depending on the applied $U$ value (e.g., $U = 6$ eV vs. $U = 8.76$ eV), the previously derived conclusion remains valid. These findings highlight the critical importance of accurately predicting local atomic structures and the associated electronic properties during defect formation, which can occur at various stages of material operation.

Table 3: **Charge transfer with point defects**: Identified Ni sites where charge transfer occur with the introduction of various defects in bulk $C2/m$ $LiNiO_2$ by various DFT functionals and methods. U=6 eV, V=0.72 eV and 0.55 eV for long and short Ni-O bond lengths, respectively. Labeling of Ni sites are marked in Fig. 4. $Ni_{1,2,3}$ are the three nearest-neighbor Ni sites to the oxygen vacancy, where $Ni_{1,2}$ sites are equivalently closer to oxygen vacancy than $Ni_3$ due to JT distortion; $Ni_5$ is the swapping Ni in Li-Ni antisite and $Ni_{4,6,7}$ are nearest-neighbor Ni sites to $Ni_5$. Only case 1 configuration of Li-Ni antisite is considered here.

| $Ni^{2+}/Ni^{4+}$ sites | PBE+U | PBE+U+V | $r^2$SCAN | SCAN | HSE06 |
|---|---|---|---|---|---|
| O vac ($Ni^{2+}$) | $Ni_{1,2,3}$ | $Ni_{1,2}$ | $Ni_{1,2}$ | $Ni_{1,2}$ | $Ni_{1,2}$ |
| Li vac ($Ni^{4+}$) | None | None | Ni in the nearest-neighbor layer | | |
| Li-Ni antisite ($Ni^{2+}$) | $Ni_{4,5,6}$ | $Ni_{4,5}$ | $Ni_{4,5}$ | $Ni_{4,5}$ | $Ni_{4,5}$ |
| Li-Ni antisite ($Ni^{4+}$) | None | $Ni_7$ | $Ni_7$ | $Ni_7$ | $Ni_7$ |

## Validation of proposed simulation protocol and discussion

Building on the previously discussed benchmark results, we propose an efficient yet accurate DFT calculation scheme for predicting the physicochemical properties of strongly correlated transition metal oxides (TMOs). This approach involves performing structural relaxation using the SCAN functional, followed by a single-step self-consistent HSE06 calculation (referred to as one-shot HSE06 or HSE06-on-SCAN in the following discussion). To validate this proposed procedure, we re-evaluate the properties discussed earlier and compare the results with those obtained from fully relaxed HSE06 calculations.

We found that HSE06-on-SCAN greatly improves the energy description compared to SCAN. As shown in Table 4, HSE06-on-SCAN provides an almost identical description to HSE06-relaxed results for energy differences between different phases of $LiNiO_2$ and defect formation energies. This improvement also enables more accurate predictions of the delithiation voltage, as shown in Fig. 5. The discrepancy observed between the one-shot HSE and fully relaxed HSE calculations in Table 4 and Fig. 5 is considered insignificant, as the voltage difference falls within the uncertainty range of the QMC prediction (Fig. 3) and the defect formation energy difference is merely $\sim$1% of the absolute values.

This is because HSE06 improves the electronic structure description on top of SCAN-

relaxed structures, as we found almost identical description between HSE06-on-SCAN and HSE06 calculations on density of states, magnetic moment, and band gap values, as summarized in Table S10 and Figs. S11 and S12. Finally, as SCAN relaxed defect structures are similar to those obtained with HSE06 relaxation, it is not surprising to see that the HSE06-on-SCAN method also leads to identical charge transfer process in defect structures (Table S11 and Fig. S13).

Table 4: Comparison of computed energies from SCAN, HSE06-on-SCAN and HSE06 methods. $\Delta E$: energy difference between $R\bar{3}m$ and $C2/m$ phases of bulk $LiNiO_2$ (note with SCAN relaxation, a hexagonal phase, instead of $R\bar{3}m$ symmetry was obtained). $E_{Ovac}$, $E_{Livac}$ and $E_{Li-Ni}$ refer to the formation energies of oxygen vacancy, Li vacancy and Li-Ni antisite in a 72-atom unit cell, respectively.

| | SCAN relaxation | HSE06 on SCAN | HSE06 relaxation |
|---|---|---|---|
| $\Delta E$ (meV/f.u.) | 50.6 | 76.4 | 62.3 |
| $E_{Ovac}$ (eV) | 3.26 | 1.99 | 1.92 |
| $E_{Livac}$ (eV) | 3.53 | 4.42 | 4.15 |
| $E_{Li-Ni-case1}$ (eV) | 0.74 | 1.27 | 1.16 |

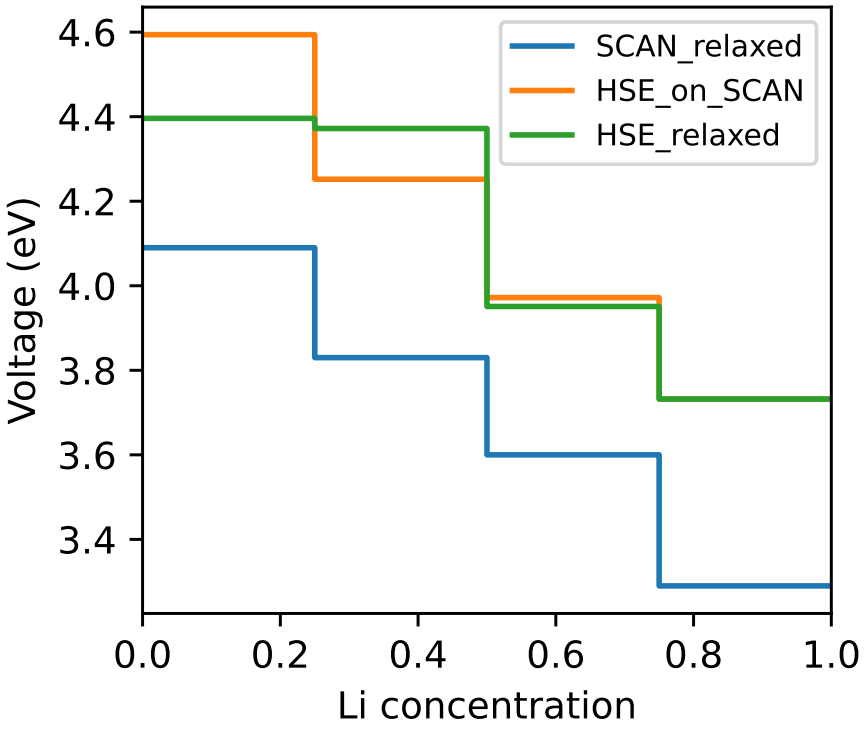


Figure 5: Comparison of delithiation voltage computed from SCAN, one-shot HSE06 and HSE06 calculations.

Next, we discuss the potential applications and limitations of this simulation protocol. One of the main advantages of our proposed protocol is its ability to effectively capture local JT distortions while providing accurate predictions for energy and electronic structures. The importance of choosing an optimal functional to capture JT distortions is currently under-emphasized. For instance, we found that using a post-correction scheme, i.e., performing a single-step HSE06 calculation on a structure relaxed at a lower level of theory (e.g., with RPBE), does not always lead to improved energy predictions. Our proposed HSE06-on-SCAN protocol, however, accurately corrects the energetics while capturing local JT distortions associated with the electronic response of TM species to their chemical environment. We expect this approach to be readily extendable to the study of other TMOs with strong JT effects, such as systems with strongly correlated open-shell TM elements with competing spin configurations,[73] systems that exhibit defect-induced dynamical evolution of

TM oxidation states,[74] and systems that undergo surface reconstructions or exhibit surface reactions with species present in operating environments.

From a technical perspective, our proposed simulation strategy substantially reduces computational costs compared to full HSE calculations, achieving approximately a seven-fold performance improvement, as highlighted in Table 5. At the same time, it maintains the desired accuracy. This enables larger-scale simulations to capture experimentally relevant conditions with high fidelity. Examples include explicitly modeling the solution environment on the surface, simulating non-dilute and non-homogeneous ion diffusion during cycling, evaluating the impact of grain boundaries, and analyzing phase evolution and segregation effects. More promisingly, given the increasing popularity of machine-learning (ML) surrogate models in battery research, our proposed simulation protocol can be leveraged to generate high-fidelity training and validation data for the development of robust ML potentials.

Table 5: Comparison of the total CPU time needed for HSE06-on-SCAN and full HSE06 for several structural relaxation calculations. The time ratio is defined as the ratio of total CPU times for HSE06-on-SCAN relative to that of full HSE06 calculations. The CPU version of VASP 5.4.4 was used for all comparisons using 224 Intel Xeon cores.

| CPU time (hours) | HSE06 on SCAN | Full HSE06 relaxation | Time ratio |
|---|---|---|---|
| Pristine bulk structure | 0.7 | 5 | 0.14 |
| 50% delithiated case | 7.8 | 29.4 | 0.26 |
| Supercell with point defects | 5.0 | 48 | 0.1 |

Finally, we acknowledge that our proposed protocol may require further validation for transport property predictions, such as the electronic conductivity and ionic conductivity of Li-ions in TMOs, which is beyond the scope of the current study. For Li diffusion barrier calculations, although promising results have been demonstrated in the literature using SCAN among GGA, SCAN, GGA+U, and SCAN+U,[35] the results can be sensitive to the degree of local structural distortions and electron localization captured by different levels of DFT theory during Li migration. For example, Loftager et al.[75] discussed the potential impact of DFT functionals on $Li^+$ diffusion barriers, particularly in relation to electron localization

at the transition state. Similarly, as mentioned in a review by Urban et al.,[76] incorrect descriptions of electron localization (e.g., by GGA+U) may result in artificial polaronic states that increase charge transfer resistance during Li migration. On the other hand, Nie et al.[77] emphasized the importance of accurately capturing JT distortions to predict electron transport behavior in $Li_xMnPO_4$. Specifically, accurately describing the band gap is a prerequisite for predicting the electronic conductivity of the material. Additional computational adjustments may be required, such as tuning the mixing parameters of the HSE functional or applying higher-level theories beyond DFT.

# Conclusions

In conclusion, we investigated three $LiNiO_2$ (LNO) systems to evaluate the performance of various DFT functionals in predicting energetics, local structural distortions, and electronic structures. A summary of the functionals' performance on tested properties can be found in Table 6. In general, each DFT exchange-correlation functional exhibits certain limitations due to the inherent challenges of treating many-body effects based on a mean-field representation of electron-electron interactions. For PBE+U+V, while an accurate description of energies and electronic structures can be achieved by adjusting U/V values, it lacks the ability to simultaneously capture local structural distortions. Furthermore, the fidelity of PBE+U+V predictions is highly dependent on the choice of U/V parameters, which poses significant challenges of parameter tuning to model materials behavior under non-uniform and dynamically evolving chemical environments. On the other hand, the SCAN functional excels at capturing local structural distortions but is less satisfactory in predicting energies and electronic structures. Finally, the HSE06 functional generally performs well but fails to reproduce the electronic band gap—a limitation that can be mitigated by tuning its mixing parameter. Since our proposed correction scheme relies on HSE-level accuracy, any inherent limitations of the HSE functional in predicting the physicochemical properties of these

strongly correlated transition metal oxide systems may be amplified.

Specifically, the conclusions regarding each functional's performance are based on three tests. First, we examined how well each functional distinguishes between the $R\bar{3}m$ and $C2/m$ phases of $LiNiO_2$, the underlying factors driving this differentiation, and the calculated band gap. Our findings reveal that the energy difference between these two phases is governed by both Ni-3$d$ and O-2$p$ orbital hybridization and the degree of JT distortion. Among the tested functionals, HSE06 most accurately captures both orbital hybridization and local structural changes, while the SCAN functional is equally effective in describing JT distortions. In contrast, the PBE+U+V correction method struggles to initiate JT distortions without symmetry breaking, although it reliably predicts Ni-3$d$ and O-2$p$ orbital hybridization. Additionally, parameter tuning is necessary for all tested functionals to reproduce the experimental band gap. For delithiated structures, we found that HSE06 and PBE+U most accurately reproduce the experimental and higher-level theoretical delithiation voltage profiles. This further demonstrates the capability of these functionals to provide precise descriptions of energetics and orbital hybridization.

Table 6: Summary of functional behavior for tested properties.

| **Properties** | **JT distortion** | **Ni-O orbital hybridization** | **Voltage/ Defect formation energies** | **Defect charge transfer** | **Band gap** |
|---|---|---|---|---|---|
| PBE+U(+V) | × | ✓ | ✓ | × | depends on U,V |
| SCAN | ✓ | × | × | ✓ | × |
| HSE06 | ✓ | ✓ | ✓ | ✓ | × |

Finally, we analyzed defect formation energies and charge transfer in defective bulk $LiNiO_2$ for three types of point defects: O vacancies, Li vacancies, and Li-Ni antisites. The formation energies predicted by HSE06 and PBE+U/V functionals were found to be similar. However, our charge transfer analysis revealed that PBE+U/V produces the most spatially delocalized charge transfer, followed by SCAN and $r^2$SCAN, with HSE06 showing

the strongest charge localization. This behavior correlates with the degree of JT distortion captured by each functional, confirming that PBE+U/V induces relatively weaker local structural distortions compared to the other functionals.

Based on these findings, we propose an efficient yet accurate DFT calculation scheme to capture local atomic structure variation and associated energetic changes in response to defect formation and chemcial reactions: structural relaxation using the SCAN functional followed by a one-shot HSE06 calculation on the relaxed structure to extract key properties. We showed the effectiveness of this HSE06-on-SCAN scheme by comparing the energetics and electronic structures against HSE06 results. Our systematic analysis provides a pathway to extend DFT-level accuracy to larger-scale simulations, offering a practical and reliable framework for studying strongly correlated transition metal oxides.

## Acknowledgement

This work was performed under the auspices of the U.S. Department of Energy by Lawrence Livermore National Laboratory under contract DE-AC52-07NA27344 and supported by the Cathode Electrolyte Interface Consortium, the Department of Energy's Office of Energy Efficiency and Renewable Energy, Vehicle Technologies Office. Computing support was provided by the Lawrence Livermore National Laboratory Institutional Computing Grand Challenge program and resources sponsored by the Department of Energy's Office of Energy Efficiency and Renewable Energy, located at the National Renewable Energy Laboratory. We thank Abdul Ghaffar, Kayahan Saritas, Jaron T. Krogel and Fernando A. Reboredo at Oak Ridge National Laboratory for helpful discussions on DMC and DFT results.

## Supporting Information Available

Correction to $O_2$ binding energies; optimized structural parameters and SCAN-relaxed structure coordinates for each case, magnetic moment of Ni and density of states analysis for

various $Li_{1-x}NiO_2$ phases; delithiation volatge calculated by different pseudopotentials, U/V values and structures.

# Author Declarations

## Conflict of Interest

The authors have no conflicts to disclose.

# References


(1) Foulkes, W. M. C.; Mitas, L.; Needs, R. J.; Rajagopal, G. Quantum Monte Carlo simulations of solids. *Rev. Mod. Phys.* **2001**, *73*, 33–83.

(2) Wagner, L. K. Transition metal oxides using quantum Monte Carlo. *J. Phys. Condens. Matter.* **2007**, *19*, 343201.

(3) Shin, H.; Gasperich, K.; Rojas, T.; Ngo, A. T.; Krogel, J. T.; Benali, A. Systematic Improvement of Quantum Monte Carlo Calculations in Transition Metal Oxides: sCI-Driven Wavefunction Optimization for Reliable Band Gap Prediction. *J. Chem. Theory Comput.* **2024**, *20*, 8175–8189.

(4) Saritas, K.; Fadel, E. R.; Kozinsky, B.; Grossman, J. C. Charge Density and Redox Potential of $LiNiO_2$ Using Ab Initio Diffusion Quantum Monte Carlo. *J. Phys. Chem. C* **2020**, *124*, 5893–5901.

(5) Georges, A.; Kotliar, G.; Krauth, W.; Rozenberg, M. J. Dynamical mean-field theory of strongly correlated fermion systems and the limit of infinite dimensions. *Rev. Mod. Phys.* **1996**, *68*, 13–125.

(6) Mandal, S.; Haule, K.; Rabe, K. M.; Vanderbilt, D. Systematic beyond-DFT study of binary transition metal oxides. *npj Compt. Mater.* **2019**, *5*, 115.

(7) Xu, S.; Luo, G.; Jacobs, R.; Fang, S.; Mahanthappa, M. K.; Hamers, R. J.; Morgan, D. Ab initio modeling of electrolyte molecule ethylene carbonate decomposition reaction on Li(Ni, Mn, Co)$O_2$ cathode surface. *ACS Appl. Mater. Interfaces.* **2017**, *9*, 20545–20553.

(8) Tebbe, J. L.; Fuerst, T. F.; Musgrave, C. B. Degradation of ethylene carbonate electrolytes of lithium ion batteries via ring opening activated by $LiCoO_2$ cathode surfaces and electrolyte species. *ACS Appl. Mater. Interfaces.* **2016**, *8*, 26664–26674.

(9) Liang, L.; Zhang, W.; Zhao, F.; Denis, D. K.; Zaman, F. U.; Hou, L.; Yuan, C. Surface/interface structure degradation of Ni-rich layered oxide cathodes toward lithium-ion batteries: fundamental mechanisms and remedying strategies. *Adv. Mater. Interfaces.* **2020**, *7*, 1901749.

(10) Li, M.; Yang, X.; Wei, X.; Zhu, Y.; Sun, X.; Gu, M. D. Cathode-Electrolyte Interphase of Ni-Rich Layered Oxides: Evolving Structure and Implication on Stability. *Nano Lett.* **2025**, *25*, 2769–2776.

(11) Rowberg, A. J.; Li, M.; Ogitsu, T.; Varley, J. B. Incorporation of protons and hydroxide species in $BaZrO_3$ and $BaCeO_3$. *Mater. Adv.* **2023**, *4*, 6233–6243.

(12) Li, Y.; Chen, C.; Ding, Y.; Wan, J.; Huang, W. Effect of grains and grain boundaries on concentrations and mobility of charge carriers in $Ba_3Ca_{1.18}Nb_{1.82}O_{9-\delta}$. *Mater. Res. Bull.* **2023**, *165*, 112299.

(13) Cui, Z.; Qi, R. First-principles simulation of oxygen evolution reaction (OER) catalytic performance of $IrO_2$ bulk-like structures: Nanosphere, nanowire and nanotube. *Appl. Surf. Sci.* **2021**, *554*, 149591.

(14) Gono, P.; Ambrosio, F.; Pasquarello, A. Effect of the solvent on the oxygen evolution reaction at the $TiO_2$–water interface. *J. Phys. Chem. C* **2019**, *123*, 18467–18474.

(15) Chakraborty, A.; Dixit, M.; Aurbach, D.; Major, D. T. Predicting accurate cathode properties of layered oxide materials using the SCAN meta-GGA density functional. *npj Compt. Mater.* **2018**, *4*, 60.

(16) Isaacs, E. B.; Patel, S.; Wolverton, C. Prediction of Li intercalation voltages in rechargeable battery cathode materials: Effects of exchange-correlation functional, van der Waals interactions, and Hubbard $U$. *Phys. Rev. Mater.* **2020**, *4*, 065405.

(17) Li, X.; Wang, Q.; Guo, H.; Artrith, N.; Urban, A. Understanding the onset of surface degradation in LiNiO2 cathodes. *ACS Appl. Energy Mater* **2022**, *5*, 5730–5741.

(18) Dudarev, S. L.; Botton, G. A.; Savrasov, S. Y.; Humphreys, C. J.; Sutton, A. P. Electron-energy-loss spectra and the structural stability of nickel oxide: An LSDA+U study. *Phys. Rev. B* **1998**, *57*, 1505–1509.

(19) Anisimov, V. I.; Zaanen, J.; Andersen, O. K. Band theory and Mott insulators: Hubbard U instead of Stoner I. *Phys. Rev. B* **1991**, *44*, 943–954.

(20) Anisimov, V. I.; Solovyev, I. V.; Korotin, M. A.; Czyżyk, M. T.; Sawatzky, G. A. Density-functional theory and NiO photoemission spectra. *Phys. Rev. B* **1993**, *48*, 16929–16934.

(21) Liechtenstein, A. I.; Anisimov, V. I.; Zaanen, J. Density-functional theory and strong interactions: Orbital ordering in Mott-Hubbard insulators. *Phys. Rev. B* **1995**, *52*, R5467–R5470.

(22) Campo, V. L.; Cococcioni, M. Extended DFT+ U+ V method with on-site and inter-site electronic interactions. *J. Phys. Condens. Matter* **2010**, *22*, 055602.

(23) Uhrin, M.; Zadoks, A.; Binci, L.; Marzari, N.; Timrov, I. Machine learning Hubbard parameters with equivariant neural networks. *npj Compt. Mater.* **2025**, *11*, 19.

(24) Cococcioni, M.; Marzari, N. Energetics and cathode voltages of Li$M$PO$_4$ olivines ($M$ = Fe, Mn) from extended Hubbard functionals. *Phys. Rev. Mater.* **2019**, *3*, 033801.

(25) Timrov, I.; Aquilante, F.; Cococcioni, M.; Marzari, N. Accurate Electronic Properties and Intercalation Voltages of Olivine-Type Li-Ion Cathode Materials from Extended Hubbard Functionals. *PRX Energy* **2022**, *1*, 033003.

(26) Himmetoglu, B.; Floris, A.; De Gironcoli, S.; Cococcioni, M. Hubbard-corrected DFT energy functionals: The LDA+ U description of correlated systems. *Int. J. Quantum Chem.* **2014**, *114*, 14–49.

(27) Gopal, P.; De Gennaro, R.; dos Santos Gusmao, M. S.; Al Orabi, R. A. R.; Wang, H.; Curtarolo, S.; Fornari, M.; Nardelli, M. B. Improved electronic structure and magnetic exchange interactions in transition metal oxides. *J. Condens. Matter Phys.* **2017**, *29*, 444003.

(28) Zhou, F.; Cococcioni, M.; Marianetti, C. A.; Morgan, D.; Ceder, G. First-principles prediction of redox potentials in transition-metal compounds with LDA + $U$. *Phys. Rev. B* **2004**, *70*, 235121.

(29) Sai Gautam, G.; Carter, E. A. Evaluating transition metal oxides within DFT-SCAN and SCAN + $U$ frameworks for solar thermochemical applications. *Phys. Rev. Mater.* **2018**, *2*, 095401.

(30) Long, O. Y.; Sai Gautam, G.; Carter, E. A. Evaluating optimal $U$ for 3$d$ transition-metal oxides within the SCAN+$U$ framework. *Phys. Rev. Mater.* **2020**, *4*, 045401.

(31) Radin, M. D.; Van der Ven, A. Simulating Charge, Spin, and Orbital Ordering: Appli-

cation to Jahn–Teller Distortions in Layered Transition-Metal Oxides. *Chem. Mater.* **2018**, *30*, 607–618.

(32) Chen, H.; Freeman, C. L.; Harding, J. H. Charge disproportionation and Jahn-Teller distortion in $LiNiO_2$ and $NaNiO_2$: A density functional theory study. *Phys. Rev. B* **2011**, *84*, 085108.

(33) Das, H.; Urban, A.; Huang, W.; Ceder, G. First-Principles Simulation of the (Li–Ni–Vacancy)O Phase Diagram and Its Relevance for the Surface Phases in Ni-Rich Li-Ion Cathode Materials. *Chem. Mater.* **2017**, *29*, 7840–7851.

(34) Chen, Z.; Zou, H.; Zhu, X.; Zou, J.; Cao, J. First-principle investigation of Jahn–Teller distortion and topological analysis of chemical bonds in $LiNiO_2$. *J. Solid State Chem.* **2011**, *184*, 1784–1790.

(35) Devi, R.; Singh, B.; Canepa, P.; Sai Gautam, G. Effect of exchange-correlation functionals on the estimation of migration barriers in battery materials. *npj Compt. Mater.* **2022**, *8*, 160.

(36) Bianchini, M.; Roca-Ayats, M.; Hartmann, P.; Brezesinski, T.; Janek, J. There and Back Again—The Journey of $LiNiO_2$ as a Cathode Active Material. *Angew. Chem. Int. Ed.* **2019**, *58*, 10434–10458.

(37) Sicolo, S.; Mock, M.; Bianchini, M.; Albe, K. And Yet It Moves: $LiNiO_2$, a Dynamic Jahn–Teller System. *Chem. Mater.* **2020**, *32*, 10096–10103.

(38) Genreith-Schriever, A. R.; Coates, C. S.; Märker, K.; Seymour, I. D.; Bassey, E. N.; Grey, C. P. Probing Jahn–Teller Distortions and Antisite Defects in $LiNiO_2$ with 7Li NMR Spectroscopy and Density Functional Theory. *Chem. Mater.* **2024**, *36*, 4226–4239.

(39) Genreith-Schriever, A. R.; Alexiu, A.; Phillips, G. S.; Coates, C. S.; Nagle-Cocco, L. A. V.; Bocarsly, J. D.; Sayed, F. N.; Dutton, S. E.; Grey, C. P. Jahn–Teller Distortions and Phase Transitions in $LiNiO_2$: Insights from Ab Initio Molecular Dynamics and Variable-Temperature X-ray Diffraction. *Chem. Mater.* **2024**, *36*, 2289–2303.

(40) Weng, M.; Pan, F.; Wang, L.-W. Wannier–Koopmans method calculations for transition metal oxide band gaps. *npj Compt. Mater.* **2020**, *6*, 33.

(41) Seo, D.-H.; Urban, A.; Ceder, G. Calibrating transition-metal energy levels and oxygen bands in first-principles calculations: Accurate prediction of redox potentials and charge transfer in lithium transition-metal oxides. *Phys. Rev. B* **2015**, *92*, 115118.

(42) Radin, M. D.; Tian, F.; Siegel, D. J. Electronic structure of $Li_2O_2\{0001\}$ surfaces. *J. Mater. Sci.* **2012**, *47*, 7564–7570.

(43) Korotin, D. M.; Novoselov, D.; Anisimov, V. I. Paraorbital ground state of the trivalent Ni ion in $LiNiO_2$ from DFT+DMFT calculations. *Phys. Rev. B* **2019**, *99*, 045106.

(44) Liao, P.; Carter, E. A. Testing variations of the GW approximation on strongly correlated transition metal oxides: hematite ($\alpha$-$Fe_2O_3$) as a benchmark. *Phys. Chem. Chem. Phys.* **2011**, *13*, 15189–15199.

(45) Kresse, G.; Furthmüller, J. Efficient iterative schemes for ab initio total-energy calculations using a plane-wave basis set. *Phys. Rev. B* **1996**, *54*, 11169 – 11186.

(46) Kresse, G.; Furthmüller, J. Efficiency of ab-initio total energy calculations for metals and semiconductors using a plane-wave basis set. *Comput. Mater. Sci.* **1996**, *6*, 15–50.

(47) Krukau, A. V.; Vydrov, O. A.; Izmaylov, A. F.; Scuseria, G. E. Influence of the exchange screening parameter on the performance of screened hybrid functionals. *J. Chem. Phys.* **2006**, *125*, 224106.

(48) Sun, J.; Ruzsinszky, A.; Perdew, J. P. Strongly Constrained and Appropriately Normed Semilocal Density Functional. *Phys. Rev. Lett.* **2015**, *115*, 036402.

(49) Furness, J. W.; Kaplan, A. D.; Ning, J.; Perdew, J. P.; Sun, J. Accurate and Numerically Efficient r$^2$SCAN Meta-Generalized Gradient Approximation. *J. Phys. Chem. Lett.* **2020**, *11*, 8208–8215, PMID: 32876454.

(50) Perdew, J. P.; Burke, K.; Ernzerhof, M. Generalized Gradient Approximation Made Simple. *Phys. Rev. Lett.* **1996**, *77*, 3865–3868.

(51) Perdew, J. P.; Burke, K.; Ernzerhof, M. Generalized Gradient Approximation Made Simple [Phys. Rev. Lett. 77, 3865 (1996)]. *Phys. Rev. Lett.* **1997**, *78*, 1396–1396.

(52) Giannozzi, P.; Baseggio, O.; Bonfà, P.; Brunato, D.; Car, R.; Carnimeo, I.; Cavazzoni, C.; de Gironcoli, S.; Delugas, P.; Ferrari Ruffino, F.; Ferretti, A.; Marzari, N.; Timrov, I.; Urru, A.; Baroni, S. Quantum ESPRESSO toward the exascale. *J. Chem. Phys.* **2020**, *152*, 154105.

(53) Giannozzi, P. et al. QUANTUM ESPRESSO: a modular and open-source software project for quantum simulations of materials. *J. Phys.: Condens. Matter* **2009**, *21*, 395502 (19pp).

(54) Giannozzi, P. et al. Advanced capabilities for materials modelling with QUANTUM ESPRESSO. *J. Phys.: Condens. Matter* **2017**, *29*, 465901.

(55) Prandini, G.; Marrazzo, A.; Castelli, I. E.; Mounet, N.; Marzari, N. Precision and efficiency in solid-state pseudopotential calculations. *npj Comput. Mater.* **2018**, *4*, 72.

(56) Zhang, H.; Zhong, Y.; Ouyang, C.; Gong, X.; Xiang, H. Theoretical study on the magnetic properties of cathode materials in the lithium–ion battery. *J. Chem. Phys.* **2023**, *158*, 124702.

(57) Timrov, I.; Marzari, N.; Cococcioni, M. HP – A code for the calculation of Hubbard parameters using density-functional perturbation theory. *Comput. Phys. Commun* **2022**, *279*, 108455.

(58) Hsieh, I.-T.; Wu, Y.; Li, B.; Qi, Y. First-principles study of the structures and redox mechanisms of Ni-rich lithium nickel manganese cobalt oxides. *Solid State Ion* **2024**, *411*, 116556.

(59) Urrego-Ortiz, R.; Builes, S.; Calle-Vallejo, F. Fast Correction of Errors in the DFT-Calculated Energies of Gaseous Nitrogen-Containing Species. *ChemCatChem* **2021**, *13*, 2508–2516.

(60) Bianchini, M.; Roca-Ayats, M.; Hartmann, P.; Brezesinski, T.; Janek, J. There and Back Again—The Journey of $LiNiO_2$ as a Cathode Active Material. *Angew. Chem.* **2019**, *58*, 10434–10458.

(61) Tuccillo, M.; Palumbo, O.; Pavone, M.; Muñoz-García, A. B.; Paolone, A.; Brutti, S. Analysis of the phase stability of $LiMO_2$ layered oxides (M= Co, Mn, Ni). *Crystals* **2020**, *10*, 526.

(62) Huang, H.; Chang, Y.-C.; Huang, Y.-C.; Li, L.; Komarek, A. C.; Tjeng, L. H.; Orikasa, Y.; Pao, C.-W.; Chan, T.-S.; Chen, J.-M.; others Unusual double ligand holes as catalytic active sites in $LiNiO_2$. *Nat. Commun.* **2023**, *14*, 2112.

(63) Bisogni, V.; Catalano, S.; Green, R. J.; Gibert, M.; Scherwitzl, R.; Huang, Y.; Strocov, V. N.; Zubko, P.; Balandeh, S.; Triscone, J.-M.; others Ground-state oxygen holes and the metal–insulator transition in the negative charge-transfer rare-earth nickelates. *Nat. Commun.* **2016**, *7*, 13017.

(64) Banerjee, H.; Aichhorn, M.; Grey, C. P.; Morris, A. J. Insulating behaviour in room temperature rhombohedral $LiNiO_2$ cathodes is driven by dynamic correlation. *J. Phys. Energy* **2024**, *6*, 045003.

(65) Genreith-Schriever, A. R.; Banerjee, H.; Menon, A. S.; Bassey, E. N.; Piper, L. F.; Grey, C. P.; Morris, A. J. Oxygen hole formation controls stability in $LiNiO_2$ cathodes. *Joule* **2023**, *7*, 1623–1640.

(66) Anisimov, V. I.; Zaanen, J.; Andersen, O. K. Band theory and Mott insulators: Hubbard U instead of Stoner I. *Phys. Rev. B* **1991**, *44*, 943 – 954.

(67) Delmas, C.; Fouassier, C.; Hagenmuller, P. Structural classification and properties of the layered oxides. *Physica B+C* **1980**, *99*, 81–85.

(68) Bianchini, M.; Roca-Ayats, M.; Hartmann, P.; Brezesinski, T.; Janek, J. There and back again—the journey of $LiNiO_2$ as a cathode active material. *Angew. Chem. Int. Ed.* **2019**, *58*, 10434–10458.

(69) Genreith-Schriever, A. R.; Coates, C. S.; Marker, K.; Seymour, I. D.; Bassey, E. N.; Grey, C. P. Probing Jahn–Teller distortions and antisite defects in $LiNiO_2$ with 7Li NMR spectroscopy and density functional theory. *Chem. Mater.* **2024**, *36*, 4226–4239.

(70) Chernova, N. A.; Nolis, G. M.; Omenya, F. O.; Zhou, H.; Li, Z.; Whittingham, M. S. What can we learn about battery materials from their magnetic properties? *J. Mater. Chem.* **2011**, *21*, 9865–9875.

(71) Mesnier, A.; Manthiram, A. Synthesis of $LiNiO_2$ at moderate oxygen pressure and long-term cyclability in lithium-ion full cells. *ACS Appl. Mater. Interfaces* **2020**, *12*, 52826–52835.

(72) Wang, L.; Maxisch, T.; Ceder, G. Oxidation energies of transition metal oxides within the GGA+ U framework. *Phys. Rev. B* **2006**, *73*, 195107.

(73) Hsieh, I.-T.; Wu, Y.; Li, B.; Qi, Y. First-principles study of the structures and redox mechanisms of Ni-rich lithium nickel manganese cobalt oxides. *Solid State Ion* **2024**, *411*, 116556.

(74) Zheng, Y.; Xie, H.; Li, J.; Hui, K. S.; Yu, Z.; Xu, H.; Dinh, D. A.; Ye, Z.; Zha, C.; Hui, K. N. Insights into the Jahn-Teller effect in layered oxide cathode materials for potassium-ion batteries. *Adv. Energy Mater.* **2024**, *14*, 2400461.

(75) Loftager, S.; García-Lastra, J. M.; Vegge, T. A density functional theory study of the ionic and electronic transport mechanisms in $LiFeBO_3$ battery electrodes. *J. Phys. Chem. C* **2016**, *120*, 18355–18364.

(76) Urban, A.; Seo, D.-H.; Ceder, G. Computational understanding of Li-ion batteries. *npj Compt. Mater.* **2016**, *2*, 1–13.

(77) Nie, Z.; Ouyang, C.; Chen, J.; Zhong, Z.; Du, Y.; Liu, D.; Shi, S.; Lei, M. First principles study of Jahn–Teller effects in $LixMnPO_4$. *Solid State Commun.* **2010**, *150*, 40–44.

# TOC Graphic

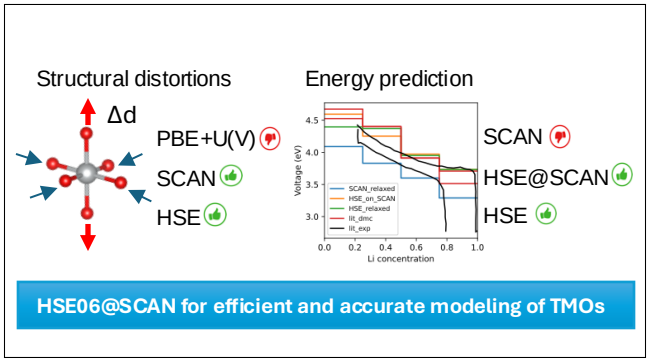
Structural distortions
Δd
PBE+U(V)
SCAN
HSE
Energy prediction
SCAN
HSE@SCAN
HSE
Voltage (eV)
Li concentration
SCAN_relaxed
HSE_on_SCAN
HSE_relaxed
lit_dmc
lit_exp
HSE06@SCAN for efficient and accurate modeling of TMOs

# Supporting Information for "Benchmarking Density Functional Theory Methods for Efficient Calculations of Strongly Correlated $Li_{1-x}Ni_{1-y}O_{2-\delta}$ System"

Shenli Zhang,[*,†,‡] Wenyu Sun,[†,‡] Eder G. Lomeli ,[†,¶] Wonseok Jeong ,[§] Stephen E. Weitzner,[†,‡] and Liwen F. Wan[*,†,‡]

†*Materials Science Division, Lawrence Livermore National Laboratory, Livermore, CA 94550, U.S.A*

‡*Laboratory for Energy Applications for the Future (LEAF), Lawrence Livermore National Laboratory, Livermore, CA 94550, U.S.A*

¶*Department of Materials Science and Engineering, Stanford University, Stanford, CA 94305, U.S.A*

§*National Institute of Standards and Technology, Gaithersburg, MD 20899, U.S.A*

E-mail: zhang52@llnl.gov; wan6@llnl.gov

## Correction of $O_2$ energy

Following Ref.,[1] we used the experimental enthalpy of the water formation reaction (-2.51 eV) to calculate the corrected energy of the $O_2$ gas molecule ($E\mathrm{corr}, \mathrm{O_2(g)}$) using the following equation:

$$E_{\mathrm{corr,O_2(g)}} = 2(E_{\mathrm{DFT,H_2O}} - E_{\mathrm{DFT,H_2}} + \Delta_f ZPE + 2.51)$$

Here, $E_{\mathrm{DFT,H_2O}}$ and $E_{\mathrm{DFT,H_2}}$ represent the DFT-computed total energies of the $H_2O$ and $H_2$ molecules, respectively, while $\Delta_f ZPE$ accounts for the vibrational zero-point energy difference between $H_2O$, $H_2$, and $O_2$ at 0 K. The corrected value of $E_{O_2}$ is provided in Table S1.

Table S1: Corrected $E_{O_2}$ for various functionals obtained using VASP PBE PAW pseudopotentials. Energies are reported in eV.

| PBE | r$^2$SCAN | SCAN | HSE06 |
|---|---|---|---|
| -9.40 | -11.42 | -11.79 | -13.35 |

Table S2: Computed structural relaxation of the C2/m $NiO_2$ cell by SCAN and HSE06 functional.

| Property | SCAN | HSE06 |
|---|---|---|
| a(Å) | 5.55 | 5.56 |
| b(Å) | 5.55 | 5.56 |
| c(Å) | 4.66 | 4.71 |
| $\alpha$ | 73.28 | 72.96 |
| $\beta$ | 73.28 | 72.96 |
| $\gamma$ | 60 | 60 |
| Ni-O bond length (Å) | 1.86 | 1.83<br>1.86 |

Table S3: Lattice parameters of $R\bar{3}m$ and $C2/m$ supercells of $LiNiO_2$ used for SCF calculations.

| structure | a (Å) | b (Å) | c (Å) | $\beta$ | Ni-O short(Å) | Ni-O long (Å) |
|---|---|---|---|---|---|---|
| $R\bar{3}m$ | 2.857 | 2.857 | 14.061 | 120 | 1.953 | 1.953 |
| $C2/m$ | 2.764 | 5.108 | 14.084 | 92.53 | 2.11 | 1.88 |

Table S4: Optimized $R\bar{3}m$ phase of $LiNiO_2$ with select DFT functionals and methods. The hexagonal supercell was used here for to facilitate comparison with experimental data. $U_1$=4.5 eV; $U_2$=6.7 eV; U+V: U=6 eV, V=0.55 eV.

| | PBE | PBE+$U_1$ | PBE+$U_2$ | PBE+U+V | r$^2$SCAN | SCAN | HSE06 |
|---|---|---|---|---|---|---|---|
| a(Å) | 2.88 | 2.89 | 2.90 | 2.92 | 2.85 | 2.85 | 2.85 |
| c(Å) | 14.18 | 14.21 | 14.27 | 14.35 | 14.05 | 14.03 | 14.025 |
| Ni-O (Å) | 1.98 | 1.99 | 2.01 | 2.00 | 1.95 | 1.88<br>1.92<br>2.04<br>(JT active) | 1.89<br>2.07<br>(JT active) |

Table S5: Optimized $C2/m$ phase of $LiNiO_2$ with select DFT functionals and methods. The primitive cell was used here to facilitate comparison with experimental data. $U_1$=4.5 eV; $U_2$=6.7 eV; U+V: U=6 eV, V=0.72 and 0.55 eV for longer and shorter Ni-O bond lengths.

| | PBE | PBE+$U_1$ | PBE+$U_2$ | PBE+U+V | r$^2$SCAN | SCAN | HSE06 |
|---|---|---|---|---|---|---|---|
| a(Å) | 2.79 | 2.79 | 2.80 | 2.88 | 2.76 | 2.76 | 2.76 |
| b(Å) | 5.16 | 5.15 | 5.17 | 5.22 | 5.10 | 5.11 | 5.11 |
| c(Å) | 5.11 | 5.107 | 5.123 | 5.166 | 5.113 | 5.06 | 5.06 |
| $\beta$ | 112.07 | 112.09 | 112.10 | 111.72 | 112.10 | 112.07 | 112.09 |
| Ni-O short (Å) | 1.91 | 1.91 | 1.92 | 1.95 | 1.89 | 1.88 | 1.87 |
| Ni-O long (Å) | 2.14 | 2.14 | 2.15 | 2.18 | 2.11 | 2.11 | 2.12 |

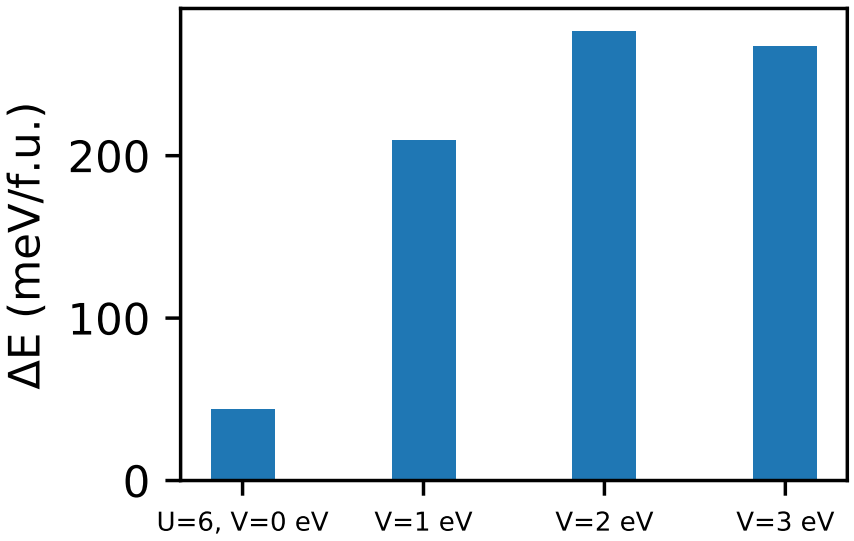


Figure S1: Computed energy difference $\Delta E = E_{R\bar{3}m} - E_{C2/m}$ as a function of V value using PBE+U+V. All data in this plot was obtained with the Quantum Espresso (QE) code. We note due to different pseudopotentials used in VASP and QE, PBE+U with the same U value in the two codes give slight different $\Delta E$ (e.g., 12.4 meV in QE versus 40 meV in VASP for U=6.7 eV).

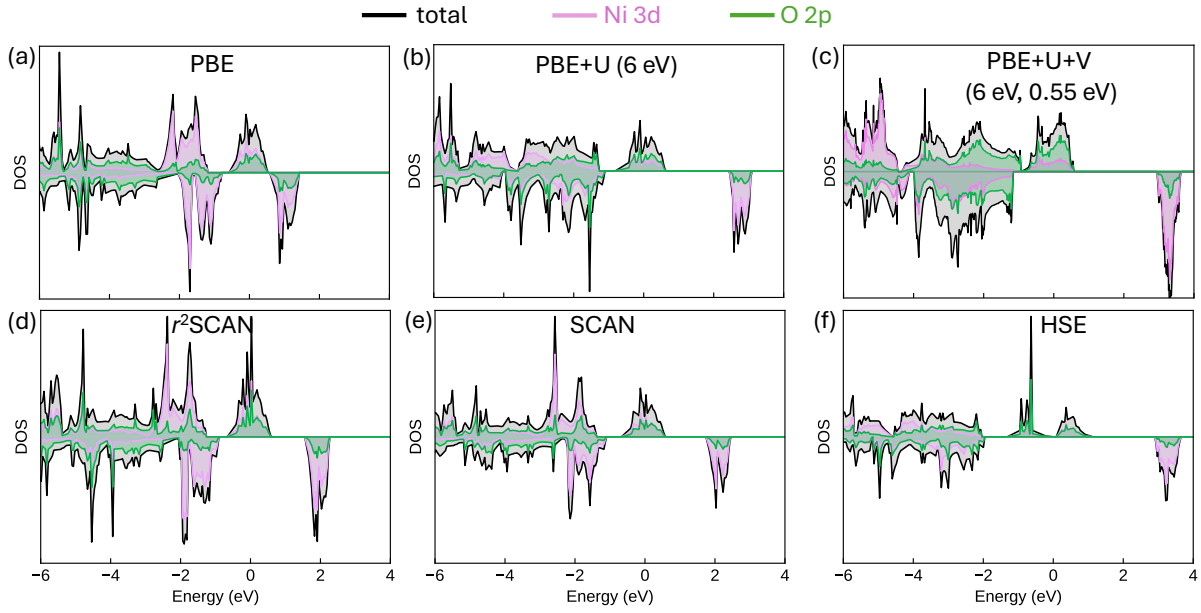


Figure S2: Projected density of states using select functionals of the PBE-relaxed $R\bar{3}m$ cell.(a)PBE; (b)PBE+U (U=6 eV); (c)PBE+U+V (U=6 eV, V=0.55 eV); (d)$r^2$SCAN; (e)SCAN; (f)HSE06.

## Discussion on Ni-3$d$ and O-2$p$ band centers

For Fig.2 in the main text, at the PBE functional level, the $d$-band center of the Ni orbitals (around -2 eV) is higher in energy than that of the O 2$p$ orbitals (<-3 eV), leading to a relatively narrow overlap between the two. Adding U and V corrections to the PBE functional makes the energy level of O 2$p$-band (between -3 eV and Fermi energy $E_F$) slightly higher than Ni 3$d$-band center (<-3 eV), and enhancing the covalency of the Ni-O bonds. Similarly, the HSE06 functional exhibits band alignment behavior comparable to PBE+U (U = 6 eV), though the relative energy shifts of the orbitals are less pronounced than those induced by U. The $r^2$SCAN and SCAN functionals, however, keeps the relative energy order between O 2$p$ (<-3 eV) and Ni 3$d$-band centers (around -2 eV) as in PBE case and slightly improves the overlap between the Ni 3$d$ and O 2$p$ orbitals.

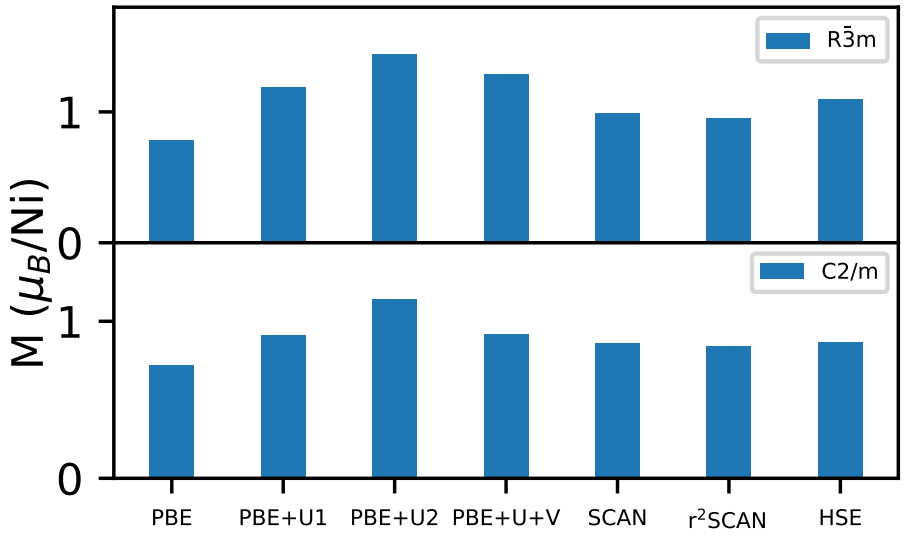


Figure S3: Magnetic moment of Ni sites in $R\bar{3}m$ and $C2/m$ phases predicted by select DFT methods. The same atomic structure obtained from PBE optimization was used for each calculation. $U_1$=4.5 eV; $U_2$=6.7 eV; U+V: U=6 eV, V=0.55 eV and 0.72 eV for shorter and longer Ni-O bond lengths.

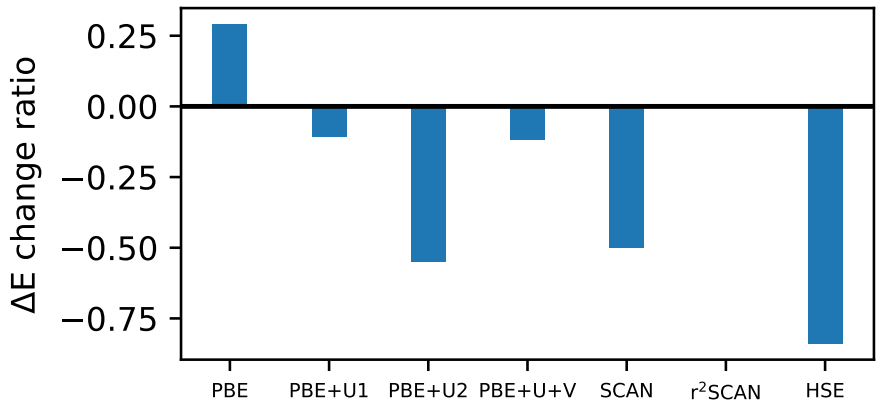


Figure S4: The $\Delta E$ change ratio with select functionals, where $\Delta E = (\Delta E_{\text{relax}} - \Delta E_{\text{SCF}})/\Delta E_{\text{SCF}}$. Here, $\Delta E_{\text{SCF}}$ is the energy difference between $R\bar{3}m$ and $C2/m$ phase without structural relaxation, $\Delta E_{\text{relax}}$ is the energy difference after structural relaxation with each functional. $U_1$, $U_2$ and U+V values are the same as in Fig. S3.

The SCAN functional produces a distinct JT distortion pattern where the top and bottom Ni layers exhibit the same elongation direction, while the middle Ni layer shows the opposite (Fig.S5a), effectively refining the crystal symmetry from rhombohedral to hexagonal. In contrast, HSE06 results in a JT distortion with a trimer pattern that preserves the rhombohedral symmetry (Fig.S5b), with this ordering achieved by initializing the calculation using a wavefunction from a PBE+U calculation while keeping the orbital ordering fixed during the HSE06 optimization. Despite differences in JT distortion patterns.

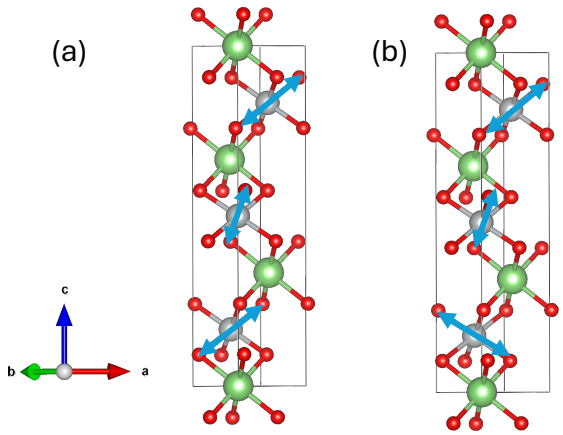


Figure S5: Jahn-Teller distortion obtained during the structural optimization of the hexagonal supercell containing the $R\bar{3}m$ phase by (a) SCAN functional (b) HSE06 functional.

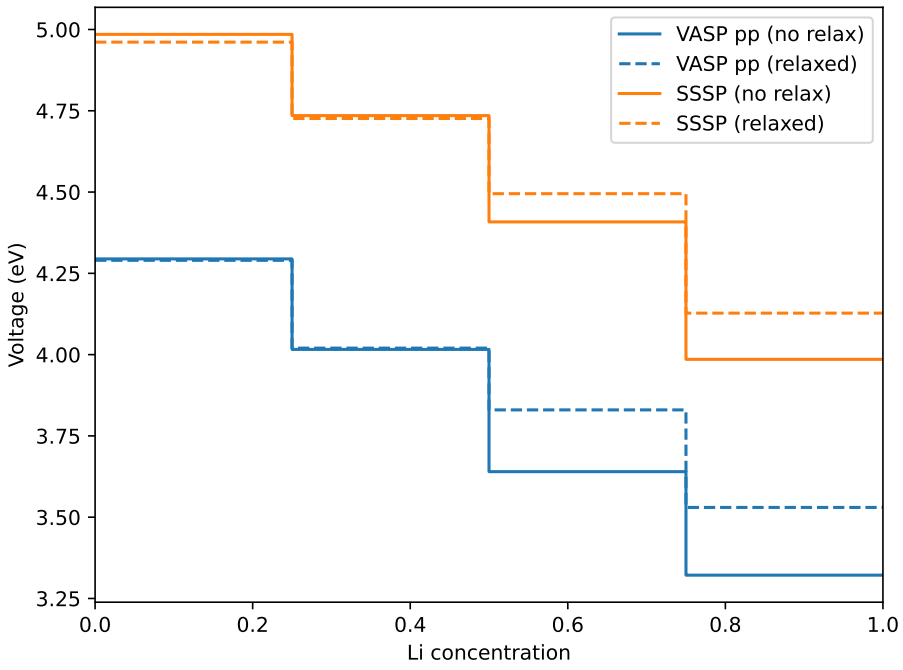


Figure S6: Calculated voltage change in $Li_{1-x}NiO_2$ as a function of Li concentration comparing VASP PAW PBE and SSSP pseudopotentials (pp). We compare two cases: 1)the same structures were used for the two pseudopotentials (no relax); 2) cell optimization was done with each pseudopotential (relaxed).

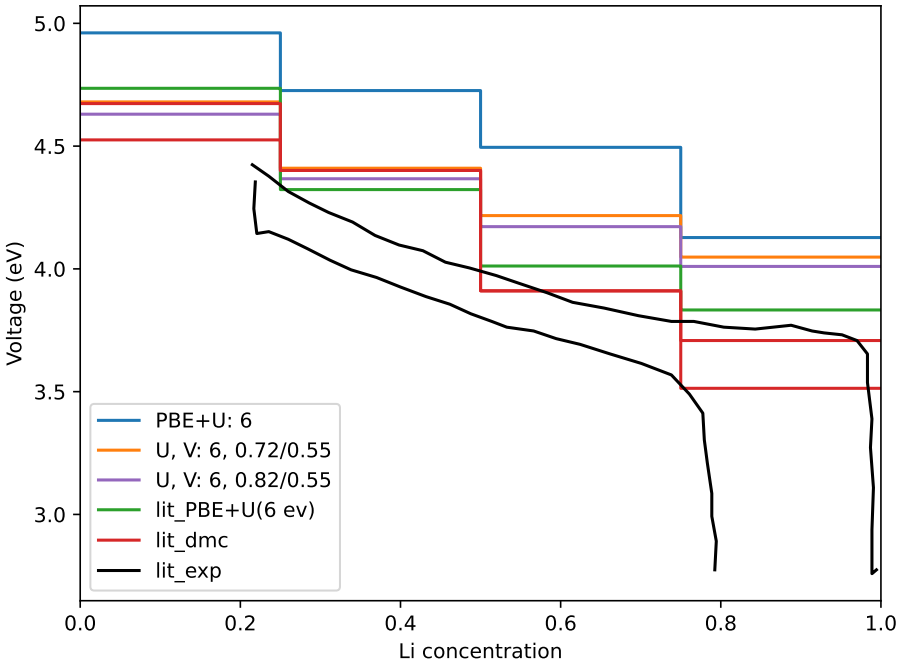


Figure S7: Calculated voltage change in $Li_{1-x}NiO_2$ as a function of Li concentration comparing PBE+U and PBE+U+V. All calculations are done using Quantum Espresso with pseudopotentials sourced from the SSSP library. Two sets of V values are tested (the two V values are for shorter and longer Ni-O bond lengths in the JT distorted $NiO_6$ units. Cell optimization was done for each structure with the corresponding U, V parameters. lit_PBE+U(6 eV), lit_exp and lit_dmc are the same reference data as in Fig.3 in the main text.

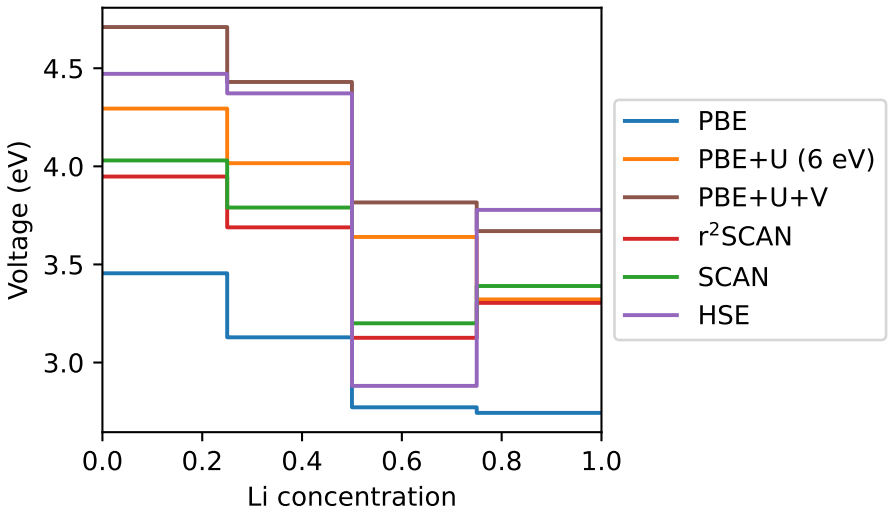


Figure S8: Calculated voltage change in $Li_{1-x}NiO_2$ as a function of Li concentration by various functionals using the same PBE-optimized structures. U=6 eV and V=0.72 and 0.55 eV.

## Determination of oxidation state of Ni

Despite a significant reduction in the band gap in the fully lithiated state ($LiNiO_2$), the insulating nature of $Li_{1-x}NiO_2$ (Fig. S9) ensures that the electronic response of Ni during Li (de)intercalation remains highly localized. The nominal charge state of Ni is commonly assigned based on its spin configuration, where a magnetic moment between 0.7 and 1.5 $\mu_B$ corresponds to the 3+ state, $\mu_B < 0.7$ corresponds to the 4+ state, and $\mu_B$ between 1.5 and 2.5 corresponds to the 2+ state (Table S6). Across all functionals, methods, and Li concentrations in our calculations of $Li_{1-x}NiO_2$, Ni consistently exhibits only two distinct magnetic moments — 0 or 1 $\mu_B$ — indicating its exclusive presence in either the 3+ or 4+ state. The ratio of $Ni^{3+}/Ni^{4+}$ increases proportionally with Li concentration, suggesting that charge compensation during Li intercalation occurs through specific neighboring Ni atoms rather than being uniformly distributed across the Ni-O octahedral layer. This behavior aligns with established mechanisms of electron conduction and charge localization in wide-band-gap semiconductors. While all DFT functionals successfully resolve the $Ni^{3+}$ state and capture the associated Jahn-Teller (JT) distortion, the predicted degree of JT distortion varies depending on the level of theory. Specifically, at $x > 0.5$, the JT distortion of $NiO_6$ octahedra, represented by the ratio of short to long Ni-O bond lengths, differs by up to 7% across DFT functionals, despite relatively small variations (within 2%) in the predicted lattice parameters (Tables S7 and S8).

Table S6: Assignment of Ni oxidation state based on magnetic moment of Ni

| Magnetic moment ($\mu_B$) | Assigned Ni oxidation state |
|---|---|
| 0-0.5 | 4+ |
| 0.5-1.5 | 3+ |
| 1.5-2.5 | 2+ |

In Tables S7 and S8, we used SCAN-optimized cell parameters for the HSE06 calculations. This choice was made because the cell parameters relaxed using the SCAN and HSE06 functionals are very similar; however, SCAN-optimized cell parameters resulted in slightly

lower energies (approximately 0.05 eV/f.u.) compared to the HSE06-optimized parameters for HSE06 calculations. Note that the internal coordinates were still relaxed using the HSE06 functional.

Table S7: Computed structural relaxation of $Li_{0.5}NiO_2$ cell with select DFT functionals. U, V values are the same as in Fig. S8. For Ni-O bond length, the first row represents the value for non-JT active Ni-O case, and the second and third rows correspond to the two bond lengths for JT distorted Ni sites.

| | PBE | PBE+U | PBE+U+J | r$^2$SCAN | SCAN | HSE06 |
|---|---|---|---|---|---|---|
| a(Å) | 5.10 | 5.10 | 5.15 | 5.10 | 5.03 | 5.03 |
| b(Å) | 5.74 | 5.74 | 5.77 | 5.74 | 5.68 | 5.68 |
| c(Å) | 5.74 | 5.74 | 5.77 | 5.74 | 5.68 | 5.68 |
| $\alpha$ | 73.91 | 73.93 | 74.38 | 73.91 | 72.63 | 72.63 |
| $\beta$ | 73.91 | 73.93 | 74.38 | 73.91 | 72.63 | 72.63 |
| $\gamma$ | 58.70 | 58.73 | 58.52 | 58.76 | 58.31 | 58.31 |
| Ni-O bond length (Å) | 1.87 | 1.87 | 1.88 | 1.86 | 1.85 | 1.88 |
| | 1.93 | 1.92 | 1.92 | 1.90 | 1.89 | 1.91 |
| | 2.10 | 2.10 | 2.13 | 2.10 | 2.09 | 2.16 |

Table S8: Computed structural relaxation of $Li_{0.75}NiO_2$ cell with select DFT functionals. U, V values are the same as in Fig. S8. For Ni-O bond length, the first row represents the value for non-JT active Ni-O case, and the second and third rows correspond to the two bond lengths for JT distorted Ni sites.

| | PBE | PBE+U | PBE+U+J | r$^2$SCAN | SCAN | HSE06 |
|---|---|---|---|---|---|---|
| a(Å) | 5.76 | 5.76 | 5.85 | 5.69 | 5.68 | 5.68 |
| b(Å) | 5.76 | 5.76 | 5.85 | 5.69 | 5.68 | 5.68 |
| c(Å) | 5.84 | 5.84 | 5.66 | 5.74 | 5.74 | 5.74 |
| $\alpha$ | 60.42 | 60.41 | 61.54 | 60.31 | 60.32 | 60.32 |
| $\beta$ | 60.42 | 60.41 | 61.54 | 60.31 | 60.32 | 60.32 |
| $\gamma$ | 60 | 60 | 60 | 60 | 60 | 60 |
| Ni-O bond length (Å) | 1.87 | 1.88 | 1.88 | 1.86 | 1.86 | 1.88 |
| | 1.96 | 1.91 | 1.89,1.97 | 1.89 | 1.89 | 1.89 |
| | 2.02 | 2.11 | 2.11 | 2.08 | 2.08 | 2.08 |

## Electronic structures of $Li_{1-x}NiO_2$

To examine the electronic structures of Li-deficient $Li_{1-x}NiO_2$ predicted by various functionals and methods, a comparison was made of the total density of states and the overlap

between Ni-3$d$ and O-2$p$ orbitals for $Ni^{4+}$ and $Ni^{3+}$ in $NiO_2$ and $Li_{0.5}NiO_2$ structures (Fig. S9). All functionals predicted both $NiO_2$ and $Li_{0.5}NiO_2$ structures to be insulating, with $Li_{0.5}NiO_2$ exhibiting a smaller band gap compared to $NiO_2$ due to the appearance of the formal $Ni^{3+}$ state (see valence and conduction band edges in Fig. S9c and S9d). However, the quantitative band gap varies significantly depending on the chosen functional. In the fully delithiated $NiO_2$ (Fig. S9a), the band gap increases progressively from PBE, to $r^2$SCAN and PBE+U (U = 6 eV), to SCAN and PBE+U+V (U = 6 eV, V = 0.72 and 0.55 eV), and finally to HSE06 functionals. For the half-delithiated $Li_{0.5}NiO_2$ (Fig. S9b), a similar trend is observed, except that PBE+U and PBE+U+V predict larger band gaps than SCAN-family functionals, akin to the $LiNiO_2$ case. Since PBE+U(+V) predicts electronic structure features similar to HSE06 for $Ni^{3+}$ sites (e.g., $d-p$ hybridization and the relative energy levels between the $d$ and $p$ bands), it is expected that PBE+U(+V) also predicts band gaps closer to HSE06 than other functionals in the $Li_{0.5/1}NiO_2$ cases. In $NiO_2$, however, where all Ni sites have a formal charge of 4+, the differences in electronic structures among the functionals are smaller than in the $Ni^{3+}$ case (Fig.S9c).

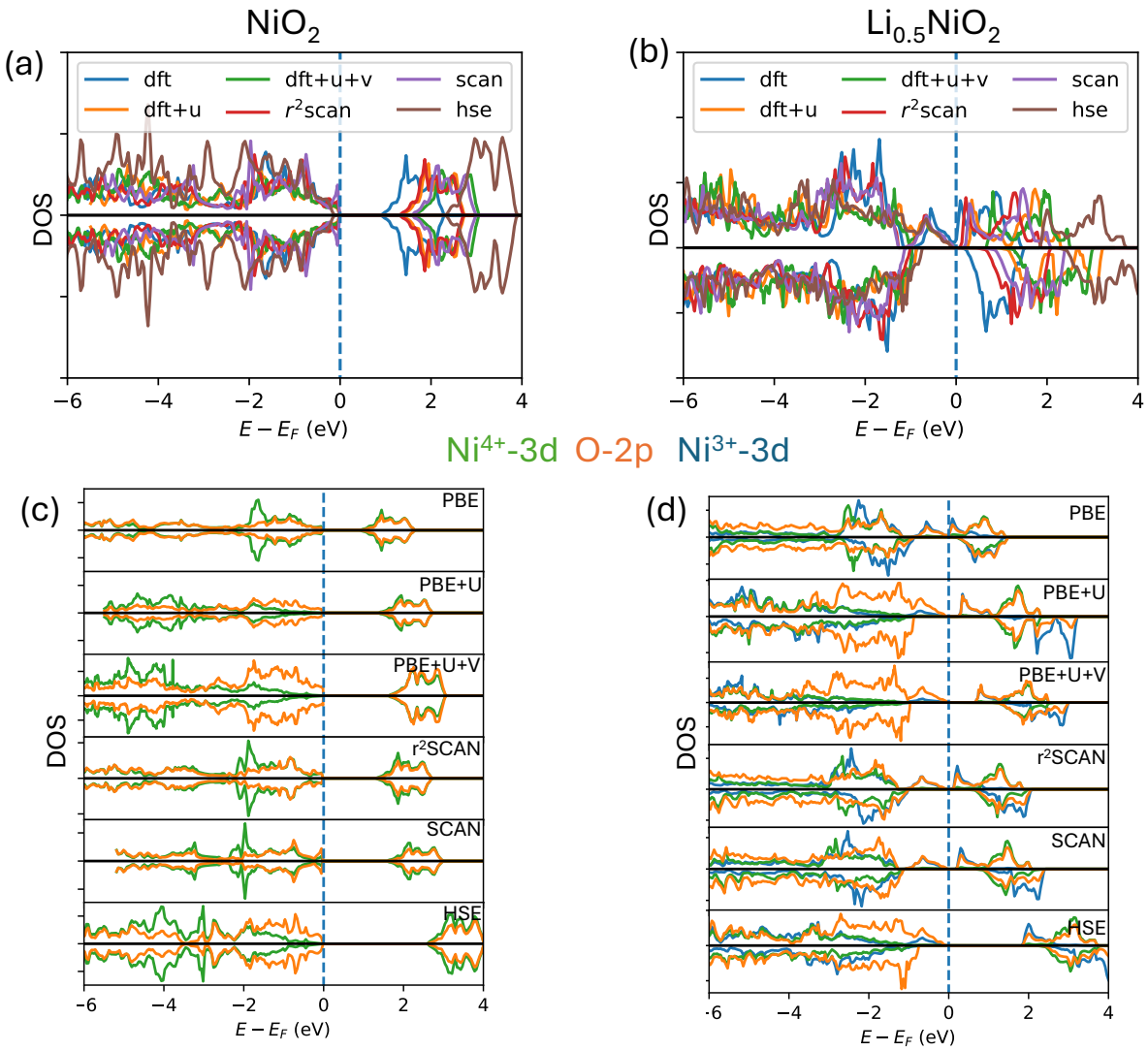


Figure S9: Computed total density of states and projected density of states of $NiO_2$ ((a) and (c)) and $Li_0.5NiO_2$ ((b) and (d)) with various functionals, all using SCAN-optimized structures.Tested functionals: PBE, PBE+U (U=6 eV), PBE+U+V (U=6 eV, V=0.72 and 0.55 eV), $r^2$SCAN, SCAN and HSE06.

Table S9: Defect formation energies calculated with U=8.76 and 6 eV respectively in bulk $LiNiO_2$ $C2/m$ phase.

| Formation energy (eV) | U=8.76 | U=6 |
|---|---|---|
| $E_{Ovac}$ | 0.18 | 1.66 |
| $E_{Livac}$ | 3.83 | 3.79 |
| $E_{Li-Ni-case1}$ | 0.04 | 0.91 |

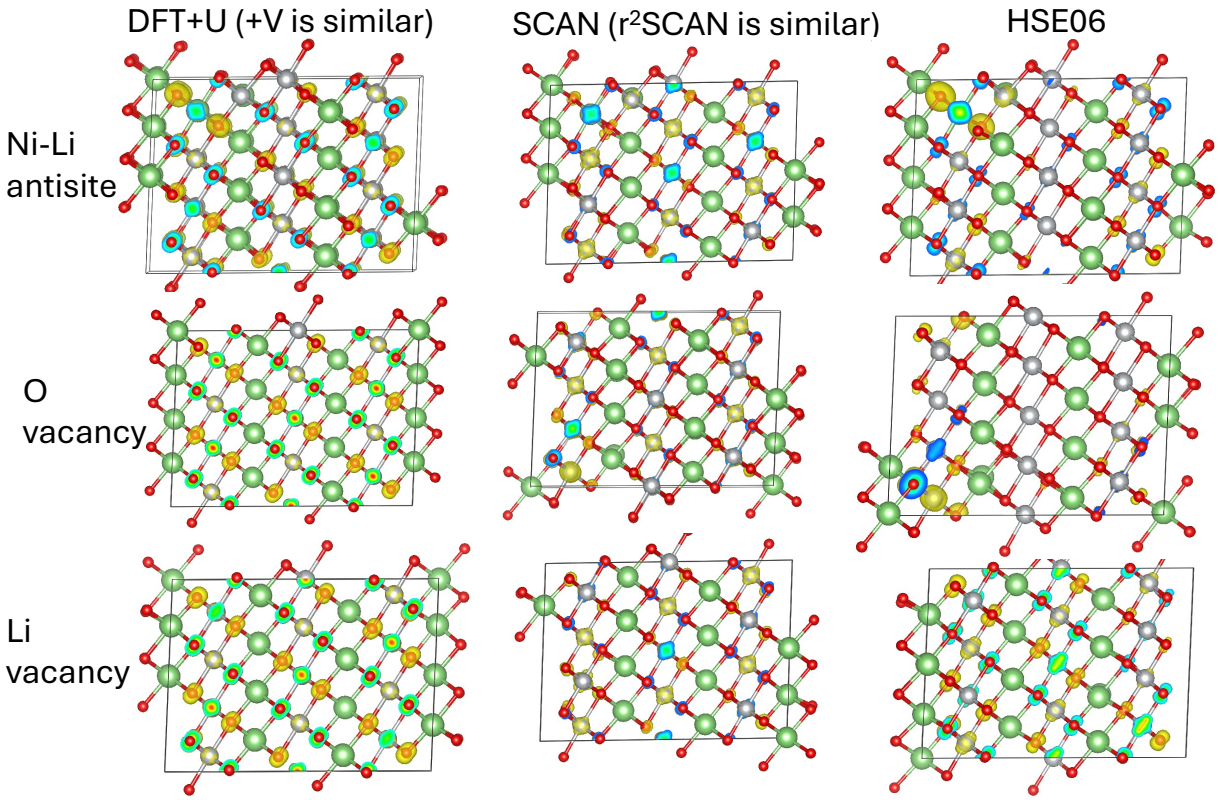


Figure S10: Comparison of computed spatial charge densities distribution for density of states within 1 eV to Fermi energy by various functionals for each defect structures.

Table S10: Comparison of computed magnetic state and band gap of $R\bar{3}m$ (or the hexagonal structure after relaxation with SCAN functional) and $C2/m$ phases of bulk $LiNiO_2$ between three different methods

| | SCAN relaxation | HSE06 on SCAN | HSE06 relaxation |
|---|---|---|---|
| M ($\mu B$/Ni)_hexagonal | 0.88, 0.90 | 0.88 | 0.88 |
| M ($\mu B$/Ni)_$C2/m$ | 0.86 | 0.87 | 0.87 |
| Band gap (eV)_hexagonal | metallic | 1.68 | metallic |
| Band gap (eV)_$C2/m$ | 0.17 | 2.08 | 2.13 |

Fig. S11 compares the density of states (DOS) of the $C2/m$ $LiNiO_2$ structure obtained using the one-shot HSE06 method and full HSE06 calculations, showing that the results are nearly identical. It is worth noting that, for the same structure, the electronic structures predicted by the SCAN functional and the HSE06 functional can differ significantly (see previous discussions on bulk $LiNiO_2$ in the main text). This demonstrates that the one-shot HSE06 method can substantially improve the quality of electronic structure descriptions. The DOS of $Li_0.5NiO_2$ and $NiO_2$ (Fig. S12) further confirms the consistency between the electronic structures obtained from the one-shot HSE06 method and full HSE06 calculations. Additionally, the atomic structures predicted by the SCAN and HSE06 functionals are found to be similar (Table S2 and S7).

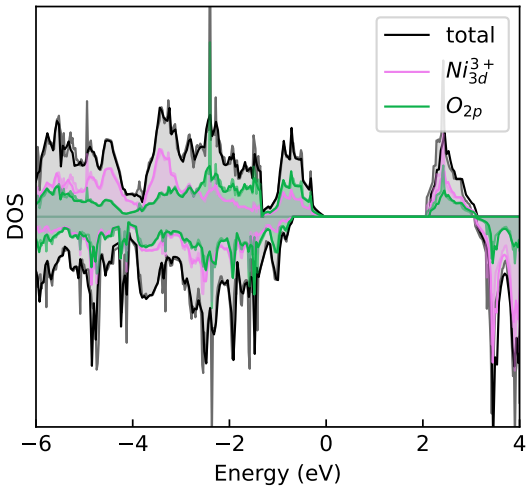


Figure S11: Comparison of computed density of states (DOS) of $LiNiO_2$ between one-shot HSE06 (solid lines) and complete HSE06 calculations (shaded area).

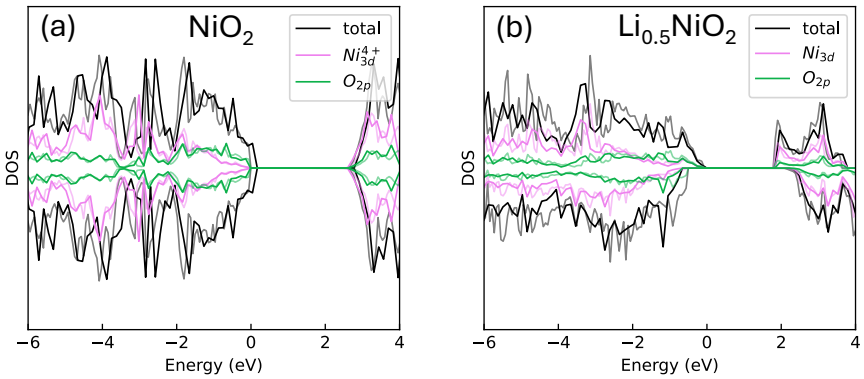


Figure S12: Comparison of computed density of states (DOS) of (a) $NiO_2$ and (b) $Li_0.5NiO_2$ between one-shot HSE06 (solid lines) and complete HSE06 calculations (transparent lines).

Table S11: **Charge transfer with point defects**: Identified Ni sites where charge transfer occur with the introduction of various defects in bulk $C2/m$ $LiNiO_2$ comparing SCAN, one-shot HSE06 and HSE06 calculations. Only case 1 configuration of Li-Ni antisite is considered here.

| $Ni^{2+}/Ni^{4+}$ sites | SCAN relaxation | HSE06 on SCAN | HSE06 relaxation |
|---|---|---|---|
| O vac ($Ni^{2+}$) | $Ni_{1,2}$ | | |
| Li vac ($Ni^{4+}$) | Ni in the nearest-neighbor layer | | |
| Li-Ni antisite ($Ni^{2+}$) | $Ni_5$ | | |
| Li-Ni antisite ($Ni^{4+}$) | $Ni_7$ | | |

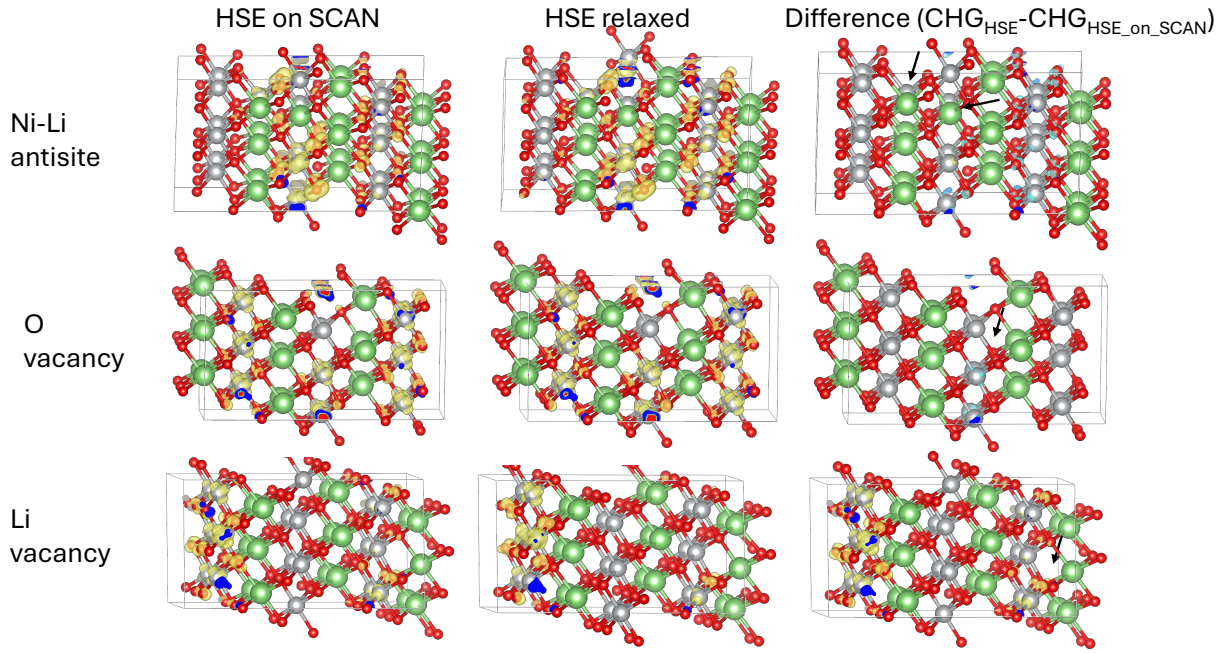


Figure S13: Comparison of computed spatial charge density distributions for density of states within 1 eV to Fermi energy by different methods. The third column of figures show the charge density difference. The same iso-surface charge density level was used to produce figures for a specific defect type.

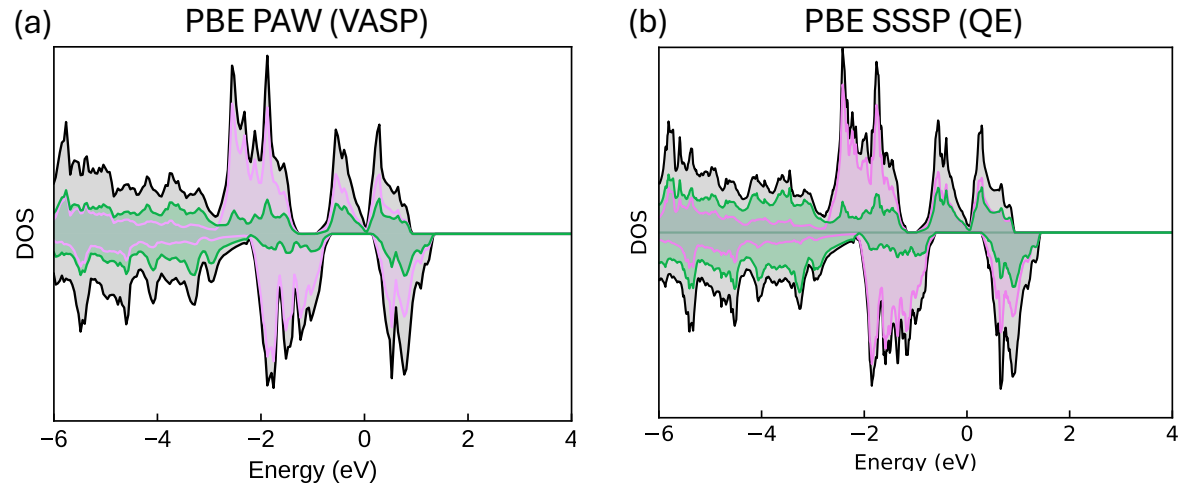


Figure S14: Comparison of computed projected density of states of the SCAN-relaxed $C2/m$ primitive cell with two different pseudopotentials (pp) using PBE functional (a) PAW pp implemented in Vienna ab initio simulation package (VASP). (b) SSSP pp, calculated with Quantum Espresso (QE) code.

SCAN-relaxed R$\bar{3}$m structure–POSCAR

| | | |
|---|---|---|
| 1.00000000000000 | | |
| 1.4253611494461274 | -2.4687979299754685 | 0.0000000000000000 |
| 1.4253611494461274 | 2.4687979299754685 | 0.0000000000000000 |
| 0.0000000000000000 | 0.0000000000000000 | 14.0290466977602684 |
| Li | Ni | O |
| 3 | 3 | 6 |
| Direct | | |
| 0.0004209598251776 | 0.0010751473920223 | 0.0000139003465094 |
| 0.6900151225911983 | 0.3545440576307115 | 0.3334664503210121 |
| 0.3096432219514895 | 0.6439064248032338 | 0.6664854436974963 |
| 0.3375948933841570 | 0.6690418530414348 | 0.1671076632698032 |
| 0.0000961895577518 | 0.0000769501910867 | 0.4999795640484948 |
| 0.6623038088815747 | 0.3309915351252641 | 0.8329076153322603 |
| 0.6263716788253006 | 0.3098639968739079 | 0.0924136282450121 |
| 0.0504753827489068 | 0.0306890709083874 | 0.2418852783232026 |
| 0.3679358696112587 | 0.7148046668931869 | 0.4251665973069265 |
| 0.6323368734232986 | 0.2856663638877777 | 0.5747911252226885 |
| 0.9491329381352287 | 0.9691422727941585 | 0.7581446352898809 |
| 0.3736730610646717 | 0.6901976604588143 | 0.9076380985967205 |

SCAN-relaxed $C2/m$ structure–POSCAR

1.00000000000000

| | | |
|---|---|---|
| 2.7621512934863031 | 0.0100522814227777 | 0.0168470045669270 |
| -0.0215932917019035 | 5.0735604208243137 | 0.5514892617298712 |
| -0.0768932017648585 | -2.1380810630009770 | 13.9089147134289224 |
| Li | Ni | O |
| 6 | 6 | 12 |

Direct

| | | |
|---|---|---|
| 0.0000509696608262 | 0.9999985058208836 | 0.0000168690200013 |
| 0.5000475045381663 | 0.4999969127157371 | 0.0000168630040989 |
| 0.5000492592427150 | 0.1682631975205595 | 0.3328013472670790 |
| 0.0000375752336694 | 0.6682780581930459 | 0.3327951510986225 |
| 0.0000450892775987 | 0.3316949412249386 | 0.6672102169410152 |
| 0.5000419505640394 | 0.8317072962501584 | 0.6672043865718607 |
| 0.9999964056263053 | 0.9999225320916167 | 0.4999667561453762 |
| 0.4999985755299079 | 0.4999229174567787 | 0.4999659810699555 |
| 0.5000296304260274 | 0.1639252971298859 | 0.8344091153232540 |
| 0.0000350066574910 | 0.6639242089551374 | 0.8344082271499005 |
| 0.0000369294236862 | 0.3360947326613797 | 0.1656145523297710 |
| 0.5000344274096165 | 0.8360966873924411 | 0.1656141396477651 |
| 0.0000010693364274 | 0.9865369175123533 | 0.2409257169788646 |
| 0.5000010765981528 | 0.4865393814489849 | 0.2409253988360192 |
| 0.0000122638715681 | 0.0134667983921943 | 0.7590886362293858 |
| 0.5000167767159382 | 0.5134646438282431 | 0.7590888092448722 |
| 0.4999315616272426 | 0.1506369140844228 | 0.5752345764489561 |
| 0.9999347458569616 | 0.6506387295342293 | 0.5752326723997072 |
| 0.5000024861214030 | 0.1845228934460366 | 0.0907396713020674 |
| 0.9999942377867796 | 0.6845225951186578 | 0.0907382856010699 |
| 0.9999725946630349 | 0.3154742590677060 | 0.9092833579405522 |
| 0.4999861090888231 | 0.8154756499689597 | 0.9092816661291394 |
| 0.9999779339322217 | 0.3492290285394546 | 0.4247172395847585 |

SCAN-relaxed $NiO_2$–POSCAR

| | | |
|---|---|---|
| 1.00000000000000 | | |
| -2.7781752467954384 | -4.8028567676237843 | 0.0301945189174502 |
| -5.5484819407581085 | -0.0045430632448358 | 0.0301940365347610 |
| -1.3641057878290777 | -0.7875669090547504 | -4.3879318912755565 |
| Ni | O | |
| 4 | 8 | |
| Direct | | |
| 0.5000059053950920 | 0.5000005229966931 | 0.9999980096602670 |
| 0.9999950524910943 | 0.4999915777275277 | 0.0000060034918192 |
| 0.4999988009889336 | 0.9999949166269317 | 0.0000030994824627 |
| 0.0000040091639661 | 0.0000021501071146 | 0.9999974758174801 |
| 0.3678057660333565 | 0.3678021998542320 | 0.7865549282171571 |
| 0.1321964357853318 | 0.1321944176247030 | 0.2134431037730593 |
| 0.8678052147266584 | 0.3678023760370337 | 0.7865592358214286 |
| 0.6321973519225565 | 0.1321945057613760 | 0.2134423475206262 |
| 0.3678023803636918 | 0.8678091764750349 | 0.7865562512076494 |
| 0.1321932392530130 | 0.6321995403885268 | 0.2134401580625536 |
| 0.8678016784792888 | 0.8678095289014252 | 0.7865553863265617 |
| 0.6321942853970128 | 0.6321989674994057 | 0.2134440886189353 |

SCAN-relaxed $Li_{0.25}NiO_2$–POSCAR

| | | |
|---|---|---|
| 1.00000000000000 | | |
| -2.7631196894869787 | 4.7875499035132156 | -0.0325812811916754 |
| 5.5978689221661941 | 0.0414907752448573 | 0.0299035298412206 |
| 2.7679311815023144 | -1.5623491007596215 | -4.7377835887134214 |
| Li | Ni | O |
| 1 | 4 | 8 |
| Direct | | |
| 0.5004329548825192 | 0.5000441470574603 | 0.4999816533992025 |
| -0.0000738012483016 | -0.0000688068029480 | 0.0000521344664542 |
| -0.0000224229246939 | 0.4999929067665990 | -0.0000017772366998 |
| 0.4999611840317268 | 0.0000223887565789 | -0.0000178891567851 |
| 0.4999586980109300 | 0.4999958191818406 | -0.0000070111388621 |
| 0.2690863668775609 | 0.7341405390698148 | 0.8003081337637048 |
| 0.2736196007782640 | 0.2367602176999753 | 0.8023693691066519 |
| 0.7482314011816588 | 0.7078465968191907 | 0.7844841769830878 |
| 0.7692718624376637 | 0.2365144903878611 | 0.8024153847103989 |
| 0.7308348765912228 | 0.2658942841976675 | 0.1996562545182776 |
| 0.7262403882569705 | 0.7632106376673197 | 0.1976365570477195 |
| 0.2517711284633454 | 0.2921809090905305 | 0.2155035059383837 |
| 0.2306878156611276 | 0.7634658391081112 | 0.1976194915984653 |

SCAN-relaxed $Li_{0.5}NiO_2$–POSCAR

| | | |
|---|---|---|
| 1.00000000000000 | | |
| 1.6345109322974267 | -0.0000035338716590 | -4.7558838944693491 |
| 4.9607152538063941 | -2.7680102204324313 | -0.0881228671308662 |
| -4.9607127306872645 | -2.7680131802471393 | 0.0881228793031708 |
| Li | Ni | O |
| 2 | 4 | 8 |
| Direct 0.0011703495582795 | 0.4979723799518558 | 0.5020251229413180 |
| 0.0011701691895873 | 0.9979719954094126 | 0.0020253708825810 |
| 0.5017561129191467 | 0.2503769259983443 | 0.7496239632706032 |
| 0.5017610472962022 | 0.7503774320036400 | 0.2496232211219649 |
| 0.4984327402880882 | 0.2507285041136520 | 0.2492723077586513 |
| 0.4984327617979457 | 0.7507280207176837 | 0.7492718733624502 |
| 0.7182849367576269 | 0.8949357161509416 | 0.1050627245178522 |
| 0.7182843673705527 | 0.3949384724387859 | 0.6050633632318146 |
| 0.6974712198217695 | 0.3769814456879901 | 0.1230170550944363 |
| 0.6974707454139362 | 0.8769833200872807 | 0.6230194615895880 |
| 0.2798118433759167 | 0.1061423080559031 | 0.8938569402677754 |
| 0.2798125039335526 | 0.6061426393944102 | 0.3938595349945072 |
| 0.3030706223861022 | 0.6228615652939810 | 0.8771412778951115 |
| 0.3030705318912902 | 0.1228592466961092 | 0.3771397370713366 |

SCAN-relaxed $Li_{0.75}NiO_2$–POSCAR

| | | |
|---|---|---|
| 1.00000000000000 | | |
| -2.8392168631590340 | -4.9222836231795499 | -0.0006240534860010 |
| -5.6823200852968982 | -0.0017241003302115 | -0.0001609255376577 |
| -2.8405950632905324 | -1.6417560428726590 | -4.7078752027068731 |
| Li | Ni | O |
| 3 | 4 | 8 |
| Direct | | |
| 0.4994717230205881 | 0.5005086522166390 | -0.0000604004630478 |
| 0.5004697876625205 | 0.0001251753896930 | 0.0003440380452708 |
| 0.0008588875491887 | 0.4996781415153154 | -0.0001715072217244 |
| 0.0007229297173378 | -0.0009310353230049 | 0.5008802085671434 |
| -0.0009402948093749 | 0.4993363215399553 | 0.5007989288506425 |
| 0.5003379004253186 | 0.5003246123962585 | 0.4988251573154390 |
| 0.4992579877666699 | 0.0007303057194663 | 0.5008613980403288 |
| 0.7535720022132035 | 0.7056499183656698 | 0.2824058043418785 |
| 0.7056016394895867 | 0.2582440433899753 | 0.2824377249846728 |
| 0.2349691651422895 | 0.2349857711564281 | 0.2949204512038219 |
| 0.2582871432401847 | 0.7535428031329379 | 0.2824273792113287 |
| 0.2463304812504049 | 0.2951287038021976 | 0.7169785857488727 |
| 0.2950268048957163 | 0.7413040852390886 | 0.7170363417601736 |
| 0.7647582022049392 | 0.7649031982742515 | 0.7053365805963989 |
| 0.7412756012314414 | 0.2464692401851271 | 0.7169793400187778 |

SCAN-relaxed $C2/m$ $LiNiO_2$ with 16 atoms–POSCAR

| | | |
|---|---|---|
| 1.00000000000000 | | |
| 4.3915552869328911 | -2.5360882377287122 | 0.6323866032838261 |
| 2.7576238575329248 | 4.7767823892418342 | 0.0051209850384155 |
| -2.1761632383002762 | 1.2513661554378166 | 4.4089089364311942 |
| Li | Ni | O |
| 4 | 4 | 8 |
| Direct | | |
| 0.5000198305638823 | 0.2499756164927288 | -0.0000170972044517 |
| 0.5000098549986649 | 0.7499765334149018 | -0.0000140527900087 |
| 0.0000181304542358 | -0.0000236335160071 | -0.0000144589825917 |
| 0.0000160865731114 | 0.4999761010066273 | -0.0000144116752266 |
| 0.4999974571837359 | 0.5000023345294277 | 0.5000222488108882 |
| 0.4999935674924510 | -0.0000204014247536 | 0.5000195933686447 |
| 0.0000068195876623 | 0.2499859226618694 | 0.5000320660308603 |
| 0.0000092756450884 | 0.7499875752716144 | 0.5000349904081516 |
| 0.7277774872592884 | 0.7500171503704366 | 0.7259040814298479 |
| 0.2721991105759901 | 0.2500136241159960 | 0.2740764169243352 |
| 0.7277724897934270 | 0.2500198264341015 | 0.7259008677560260 |
| 0.2722098546554378 | 0.7500143394316455 | 0.2740882890997868 |
| 0.2277799651453893 | 0.5000211548124838 | 0.7259050395356553 |
| 0.7722059013271910 | 0.0000151872014846 | 0.2740869001110805 |
| 0.2277797154745178 | 0.0000214074793652 | 0.7259043809738388 |
| 0.7722044482699211 | 0.5000171607180718 | 0.2740851462031777 |

SCAN-relaxed oxygen vacancy cell–POSCAR

| | | |
|---|---|---|
| 1.00000000000000 | | |
| 5.6279057687719991 | 0.0000085676050724 | 0.0000069649867212 |
| 0.0000155938106925 | 10.3284665223652024 | 0.0066321858920101 |
| 0.0000164294347165 | -0.6229297616965224 | 14.2945003908937185 |
| Li | Ni | O |
| 24 | 24 | 47 |
| Direct | | |
| 0.4999911771860678 | 0.0071616728703162 | 0.0022431026086975 |
| 0.5000441063220088 | 0.4974131021901428 | 0.0004463226934453 |
| 0.0002007333145608 | 0.0064749331708238 | 0.9991850308758905 |
| -0.0000013309426216 | 0.4964868762670739 | 0.0015884495686314 |
| 0.2481434161972015 | 0.2461724489660567 | 0.0008509976871815 |
| 0.2511905473828906 | 0.7499146344265099 | -0.0000925515381678 |
| 0.7519302485832323 | 0.2463091283733513 | 0.0009102726962534 |
| 0.7488816285468417 | 0.7500023327142893 | -0.0000940394488329 |
| 0.2497959045867057 | 0.0831208242120798 | 0.3340745610374848 |
| 0.2504058959609509 | 0.5844293807183010 | 0.3313250114586968 |
| 0.7502303165264065 | 0.0831121634632845 | 0.3340709728956478 |
| 0.7496184559187347 | 0.5844274571181107 | 0.3313252354117398 |
| 0.5000135754150410 | 0.3333509545400420 | 0.3336656700572539 |

| | | |
|---|---|---|
| 0.5000196849418591 | 0.8343182215982788 | 0.3317946737236737 |
| 0.0000172079147204 | 0.3333634232062689 | 0.3338315555807845 |
| 0.0000051800645773 | 0.8345588951165596 | 0.3315811107922432 |
| 0.5002243771973727 | 0.1585846314077139 | 0.6709705598643071 |
| 0.4999556191850136 | 0.6606971086597996 | 0.6653544327197386 |
| 0.2535117774952639 | 0.4200652425890513 | 0.6665479517373863 |
| 0.2776878678654237 | 0.9072120071017147 | 0.6606886806028767 |
| 0.7465059899901696 | 0.4201002490036312 | 0.6665582734811089 |
| 0.7225637000977543 | 0.9073139649972072 | 0.6607119158906549 |
| 0.0000414259011400 | 0.1877165784253031 | 0.6621421763036214 |
| 0.0000414129833628 | 0.6676806987718961 | 0.6649667699624842 |
| 0.4999941622574772 | 0.0016681704219777 | 0.5011020354799929 |
| 0.4999922367881789 | 0.4993888571737109 | 0.4983798683560129 |
| -0.0000047917307310 | 0.0006502695233321 | 0.5016130314604460 |
| -0.0000095789556646 | 0.4994059261989381 | 0.4985502290713898 |
| 0.2502557858791574 | 0.2512008243443617 | 0.5014217413504525 |
| 0.2498080950630617 | 0.7492158400156507 | 0.4980673294087005 |
| 0.7497350283084838 | 0.2511987425330193 | 0.5014187750548512 |
| 0.7501749447515944 | 0.7492177219981435 | 0.4980670860263540 |
| 0.2616592349719913 | 0.0845034464543386 | 0.8388886067567510 |
| 0.2499732450247240 | 0.5802435460750072 | 0.8317260105823727 |
| 0.7396282088554146 | 0.0844759048698858 | 0.8394455002661390 |

| | | |
|---|---|---|
| 0.7500122660804130 | 0.5802442864863109 | 0.8317403595394904 |
| 0.5000265756559601 | 0.3299112989076828 | 0.8362050291911903 |
| 0.5000253292798761 | 0.8337006682229887 | 0.8303399680032404 |
| 0.0000316763171121 | 0.3289385024219333 | 0.8361952671587730 |
| 0.0000020776858899 | 0.8262177397631738 | 0.8351298921813447 |
| 0.4999976102260427 | 0.1666787693350956 | 0.1690347862023129 |
| 0.5000091425638754 | 0.6666672004716259 | 0.1649543559433938 |
| 0.2500025650816203 | 0.4166529857070101 | 0.1689377221242280 |
| 0.2499127789603789 | 0.9169369215310340 | 0.1653210089584580 |
| 0.7499869504417568 | 0.4166526895694574 | 0.1689402876359506 |
| 0.7500737988129744 | 0.9169309658793490 | 0.1653110805610987 |
| -0.0000070562897293 | 0.1664035606636342 | 0.1692053442280547 |
| -0.0000166360029124 | 0.6666755901229917 | 0.1649680086464281 |
| 0.5000397926941282 | 0.4929575345976351 | 0.2414954885089826 |
| 0.5000583836938276 | 0.9896971821782612 | 0.2401250682124966 |
| 0.2500666658168948 | 0.2410896821270234 | 0.2429611498145108 |
| 0.2501286486856678 | 0.7416236981887618 | 0.2383799062922867 |
| 0.7500108798392681 | 0.2410995976901086 | 0.2429633336796304 |
| 0.7499533556842332 | 0.7416298445881508 | 0.2383777236097194 |
| 0.4999653130023515 | 0.5057660943461511 | 0.7560074231664853 |
| 0.2483756788607043 | 0.2502891607386654 | 0.7632898770426835 |
| 0.2462541181567966 | 0.7599333686584848 | 0.7572047811382498 |

| | | |
|---|---|---|
| 0.7519624277619801 | 0.2502927037031751 | 0.7634516525936446 |
| 0.7535525276067611 | 0.7598969802431114 | 0.7573614748882753 |
| 0.2474405174314490 | 0.0739980542724625 | 0.5767747287683241 |
| 0.2502106357173873 | 0.5748638516965640 | 0.5716749794161803 |
| 0.7526639458189569 | 0.0740236177985523 | 0.5767330301216415 |
| 0.7498546281684043 | 0.5748712127960038 | 0.5716804953930605 |
| 0.5000660424699390 | 0.3254544346555143 | 0.5744212110441044 |
| 0.5000689414018364 | 0.8218995758897083 | 0.5720628788760048 |
| 0.0000301948712149 | 0.3280691441638005 | 0.5748687482481218 |
| 0.0000230034746362 | 0.8240739646297447 | 0.5731563362688835 |
| 0.2495905155192900 | 0.0922970224083483 | 0.0954875027446110 |
| 0.2499829033879521 | 0.5916291244593969 | 0.0918193078573516 |
| 0.7505317911618310 | 0.0923168160261707 | 0.0954830697519993 |
| 0.7500976481499446 | 0.5916437298395291 | 0.0918199989664604 |
| 0.5000452017640807 | 0.3425943325309898 | 0.0962099719513964 |
| 0.5000298837588608 | 0.8429642758167799 | 0.0904937290878977 |
| 0.5000631586947537 | 0.1681920467876292 | 0.9196936378382383 |
| 0.5000278356621791 | 0.6565335474527211 | 0.9034259902195860 |
| 0.0005110329197204 | 0.1600489343224067 | 0.9117204272450380 |
| 0.0001459877058208 | 0.6604616681881492 | 0.9054239580802783 |
| 0.2496802931891426 | 0.4109614517845439 | 0.9059866870221721 |
| 0.2479084098545774 | 0.9105111227556711 | 0.9025377017836379 |

| | | |
|---|---|---|
| 0.7502709449870211 | 0.4110120399122363 | 0.9060506384222732 |
| 0.7526313235075373 | 0.9105659066811639 | 0.9027377100690610 |
| 0.5000261235322745 | 0.1745699407609735 | 0.4285171332762036 |
| 0.5000297487173863 | 0.6751631704284035 | 0.4240037818385122 |
| 0.0000478004254683 | 0.1762265613362370 | 0.4287378777263122 |
| 0.0000439676096935 | 0.6758553588433769 | 0.4244239969511907 |
| 0.2500166345916868 | 0.4239117126158374 | 0.4258121859358988 |
| 0.2504091564588082 | 0.9271279590161881 | 0.4270894514136150 |
| 0.7500634417004709 | 0.4239233973672775 | 0.4258104712613182 |
| 0.7496639997191140 | 0.9271263694572455 | 0.4270755102414713 |
| 0.0000370057663794 | 0.3419285821880240 | 0.0954228342991409 |
| 0.0000748861859998 | 0.8432137330197224 | 0.0911905774514104 |
| 0.0000454044269436 | 0.4927320131767648 | 0.2412849857506526 |
| 0.0000331228901529 | 0.9900900594276153 | 0.2407262420693370 |
| 0.5007931929678346 | -0.0004632612433325 | 0.7529004162705540 |
| -0.0000506568281863 | 0.5078619335112809 | 0.7583472991645498 |

SCAN-relaxed Li vacancy cell–POSCAR

| | | |
|---|---|---|
| 1.00000000000000 | | |
| 5.6028014274399034 | 0.0000004390115158 | 0.0000002325074458 |
| 0.0000007868876204 | 10.3011808423016635 | -0.0050832818181460 |
| 0.0000003759597935 | -0.6337387571571881 | 14.3075919308629409 |
| Li | Ni | O |
| 23 | 24 | 48 |
| Direct | | |
| 0.4943054355889326 | 0.5010679893319587 | 0.0005989786356453 |
| -0.0008351532561375 | 0.9991166219558453 | 0.9955925984966744 |
| 0.0002243005216165 | 0.5107317246020538 | 0.9959710185847659 |
| 0.2550751418848731 | 0.2395600771761377 | -0.0018560577277543 |
| 0.2562096178550063 | 0.7614943285696207 | 0.9959448318617521 |
| 0.7441550910478466 | 0.2396827456334606 | -0.0015899410050470 |
| 0.7405214518613294 | 0.7625639993527163 | 0.9960691158653898 |
| 0.2499539764912512 | 0.0832376275883782 | 0.3350968038312357 |
| 0.2521985249095584 | 0.5818998585008266 | 0.3339987621895641 |
| 0.7501870974770145 | 0.0836519925617940 | 0.3351375401962384 |
| 0.7505420070111640 | 0.5842684050475014 | 0.3335528838101102 |
| 0.5002264592942149 | 0.3314765343217869 | 0.3373379847022766 |
| 0.5051818264833029 | 0.8321072751926974 | 0.3312136229395454 |

| | | |
|---|---|---|
| 0.0001155340062132 | 0.3331963250175302 | 0.3362054477392560 |
| 0.0012035786859766 | 0.8232846083869999 | 0.3362323554373286 |
| 0.5004879773948169 | 0.1661461026574545 | 0.6679355127623321 |
| 0.4997708657711530 | 0.6669153028131422 | 0.6683151836091816 |
| 0.2501291688019007 | 0.4161001223662371 | 0.6688436155883806 |
| 0.2497956798970683 | 0.9160531042201264 | 0.6665891396853537 |
| 0.7505383174089612 | 0.4159839519933550 | 0.6688792481331882 |
| 0.7495801791957342 | 0.9161182713036481 | 0.6665658886410756 |
| -0.0000961734344238 | 0.1661872304815775 | 0.6680253456183718 |
| -0.0003178354750703 | 0.6658371513986850 | 0.6678155129300596 |
| 0.5000240583214506 | 0.9976339103727304 | 0.4982395363736933 |
| 0.5014099897042668 | 0.4989395739943269 | 0.4997675831359812 |
| 0.0000368691004257 | 0.9979515793276715 | 0.4984362726053214 |
| 0.0013865820570282 | 0.4987746639783817 | 0.4995898163044500 |
| 0.2513714663461825 | 0.2488226385709863 | 0.4998027080769722 |
| 0.2502852624078712 | 0.7484075073487191 | 0.4986911449674558 |
| 0.7513055549572947 | 0.2488218773680630 | 0.4998417867170562 |
| 0.7500782581175258 | 0.7483582901334500 | 0.4987483228089680 |
| 0.2503783977832185 | 0.0827235621827148 | 0.8344163571871940 |
| 0.2500340932622144 | 0.5837628059726371 | 0.8349226151313973 |
| 0.7494958193314629 | 0.0827246881297766 | 0.8344356749055837 |
| 0.7495999040202508 | 0.5837054037703621 | 0.8349060399642338 |

| | | |
|---|---|---|
| 0.4999345951999118 | 0.3336991133905495 | 0.8351607873500081 |
| 0.4999075346549520 | 0.8346189764463904 | 0.8314606949321668 |
| -0.0000955568401750 | 0.3338234689763557 | 0.8351663067864743 |
| -0.0001133072094145 | 0.8326314033560598 | 0.8299853871689827 |
| 0.4997298627803729 | 0.1667416595989070 | 0.1683281585777872 |
| 0.4990472460984448 | 0.6669217133100975 | 0.1669416539510432 |
| 0.2488204809268790 | 0.4167664654626912 | 0.1685501525131824 |
| 0.2513920678547827 | 0.9195892612819629 | 0.1633165859225857 |
| 0.7488125291564193 | 0.4161537846776376 | 0.1691118053543113 |
| 0.7500969493226843 | 0.9165870982054605 | 0.1647785415952852 |
| -0.0005007107637669 | 0.1678340274449467 | 0.1694957927182118 |
| -0.0005640709295771 | 0.6673207936524672 | 0.1657120863790394 |
| 0.5000861982692255 | 0.5031414437636758 | 0.2392463249127338 |
| 0.5002157507214685 | 0.9898293733067103 | 0.2375259319749169 |
| 0.2518842303770779 | 0.2411755339802390 | 0.2431336569138527 |
| 0.2514978318929637 | 0.7421521674326845 | 0.2381975458751241 |
| 0.7482568028076735 | 0.2409702356357326 | 0.2436768405246687 |
| 0.7671481464115993 | 0.7505524712139570 | 0.2427350990457889 |
| 0.5000701164962396 | 0.5081955385586197 | 0.7616331881133005 |
| 0.2497523301454329 | 0.2611049800086414 | 0.7598088006997751 |
| 0.2522153754828365 | 0.7569689837570437 | 0.7573378710770300 |
| 0.7510648827097058 | 0.2610505327072268 | 0.7597569012015282 |

| | | |
|---|---|---|
| 0.7475120188189969 | 0.7570317817512512 | 0.7573490317934000 |
| 0.2504428857852791 | 0.0725947896593908 | 0.5720571268024780 |
| 0.2513051559061501 | 0.5737630256589350 | 0.5731038585179117 |
| 0.7499563307806779 | 0.0729133555884663 | 0.5722743332457804 |
| 0.7513629344500845 | 0.5739801793264189 | 0.5731600969475527 |
| 0.5016070660966871 | 0.3237651868770065 | 0.5733563666974805 |
| 0.4998191845814232 | 0.8242155156281401 | 0.5716456225158572 |
| 0.0017094651080257 | 0.3238519676808261 | 0.5733047675543376 |
| -0.0002208671512090 | 0.8237680547405204 | 0.5718549099384254 |
| 0.2431710928246659 | 0.0966461142906185 | 0.0960673737672146 |
| 0.2333326513954190 | 0.5813983254482851 | 0.0917320939130085 |
| 0.7550822292010775 | 0.0962431320332694 | 0.0966882900513504 |
| 0.7464902136107618 | 0.5908423360047819 | 0.0957393251511322 |
| 0.4988837428499905 | 0.3428023087127094 | 0.0971381221749343 |
| 0.5001675493678029 | 0.8260362676076654 | 0.0978150838911468 |
| 0.4999439834316003 | 0.1646273800090902 | 0.9039525246368370 |
| 0.4994985989680035 | 0.6592867522827799 | 0.9082865592296774 |
| -0.0001246808764490 | 0.1579146354901563 | 0.9080090315886673 |
| -0.0007041522794353 | 0.6597702265075934 | 0.9070809082529485 |
| 0.2486603677968448 | 0.4081502096107213 | 0.9095162127124883 |
| 0.2447558091507810 | 0.9070274975318747 | 0.9031491514366925 |
| 0.7503170385637687 | 0.4084866264158520 | 0.9096929138473030 |

| | | |
|---|---|---|
| 0.7549599840064056 | 0.9071483979043459 | 0.9031122566152388 |
| 0.5007332980487778 | 0.1741219254513410 | 0.4255137355004897 |
| 0.5008299460459332 | 0.6737406145423378 | 0.4249702527588770 |
| 0.0007207145753825 | 0.1745171195037182 | 0.4256965382599733 |
| 0.0011444267116927 | 0.6726532200131282 | 0.4251923955051327 |
| 0.2519056446011350 | 0.4239774783748878 | 0.4254794663517396 |
| 0.2490319755731928 | 0.9236504359601549 | 0.4233964221203927 |
| 0.7507319842816050 | 0.4241315520400848 | 0.4256536318809480 |
| 0.7508066202181432 | 0.9242714008366529 | 0.4238411389769408 |
| -0.0032098776996401 | 0.3225644704944370 | 0.1021559171224014 |
| 0.0010404073646360 | 0.8450461033504171 | 0.0918490019114259 |
| -0.0009535177039567 | 0.4891998254669874 | 0.2415053633446801 |
| 0.0019004975590806 | 0.0108546136120434 | 0.2341173061925367 |
| 0.4999057843857846 | 0.0100447163206064 | 0.7589114735302964 |
| 0.0001528819734736 | 0.5085177739889355 | 0.7609244601052924 |
| -0.0000123107236829 | 0.0092982140392910 | 0.7588322797717623 |

SCAN-relaxed Li-Ni antisite cell 1–POSCAR

| | | |
|---|---|---|
| 1.00000000000000 | | |
| 5.5966022035565208 | 0.0000000000000000 | 0.0000000000000000 |
| 0.0000000000000000 | 10.3403040580396208 | 0.0000000000000000 |
| 0.0000000000000000 | -0.6272774369044152 | 14.2424985948558618 |
| Li | Ni | O |
| 24 | 24 | 48 |
| Direct | | |
| 0.5009905111449027 | 0.9991988693891235 | 0.9933300314100205 |
| 0.4995868903561929 | 0.5052750033108897 | -0.0001479439041075 |
| 0.0017760473065868 | 0.9986849785591073 | 0.9960868368830657 |
| -0.0006026140561259 | 0.5039203836301976 | 0.0009118328512974 |
| 0.2500586476698942 | 0.2393708945166246 | 0.0043981298022952 |
| 0.2535339147408774 | 0.7584330141823898 | 0.9962053171134801 |
| 0.7432029334689217 | 0.2455142021944900 | 0.0014008433638046 |
| 0.7480740742758410 | 0.7599583176977306 | 0.9966033364467074 |
| 0.2494366416989701 | 0.0816305249552780 | 0.3333109871501334 |
| 0.2498048435467325 | 0.5853342127411045 | 0.3328783699866363 |
| 0.7501634210660992 | 0.0822574044936918 | 0.3335171989637130 |
| 0.7498303623073939 | 0.5877953083376282 | 0.3319917201736293 |
| 0.4989966181328452 | 0.3346270393431539 | 0.3322824060645105 |

| | | |
|---|---|---|
| 0.4992585684490535 | 0.8311408111877036 | 0.3330106268063133 |
| 0.0004877086659104 | 0.3345691476501964 | 0.3323288333247361 |
| 0.0006075854642109 | 0.8311686435067992 | 0.3329751910880250 |
| 0.4999728575287492 | 0.1667139656074764 | 0.6703227318694376 |
| 0.4987676404125022 | 0.6712199638014552 | 0.6717660856108206 |
| 0.2497028834072668 | 0.4221941925903105 | 0.6636680786467364 |
| 0.2536557788691700 | 0.9191387810925142 | 0.6670421115360035 |
| 0.7498449919670356 | 0.4211490931521630 | 0.6629988866127796 |
| 0.5019491589478973 | 0.8333842800493813 | 0.8348343857099227 |
| 0.0022237417696549 | 0.1636329194986214 | 0.6693399871442289 |
| 0.0009472947115366 | 0.6677692878355871 | 0.6685410525992277 |
| 0.4994823512822508 | -0.0018919138516627 | 0.5013955422281060 |
| 0.4999365001770845 | 0.4989924179210214 | 0.4986291837571162 |
| 0.0001181184443934 | -0.0029896882774194 | 0.5019217088426270 |
| 0.0001202438763832 | 0.4991489142564428 | 0.4985342028194538 |
| 0.2499615614521364 | 0.2476150388302047 | 0.5027188053226812 |
| 0.2500113474331433 | 0.7484425044307040 | 0.5004190678668342 |
| 0.7499563451171544 | 0.2514677166920846 | 0.5014488948186598 |
| 0.7502604751657774 | 0.7478608164954084 | 0.4990677919884917 |
| 0.2513271894894420 | 0.0781070521535996 | 0.8356130722416193 |
| 0.2493612304251818 | 0.5850939348866877 | 0.8312885487108127 |
| 0.7504001090909227 | 0.0820479335589694 | 0.8360200370041148 |

| | | |
|---|---|---|
| 0.7480419147401932 | 0.5844272928442922 | 0.8312601283699296 |
| 0.4997936547433403 | 0.3314484091667182 | 0.8352829220456925 |
| 0.7481263354595431 | 0.9122189830846518 | 0.6701599309125384 |
| -0.0001114371032323 | 0.3324559318942407 | 0.8340784508658448 |
| 0.0034440480921944 | 0.8349821850820868 | 0.8321061154741162 |
| 0.4996861793010627 | 0.1676508305529094 | 0.1672544513081199 |
| 0.4999320819615034 | 0.6672638362535146 | 0.1650855685998472 |
| 0.2499691832522449 | 0.4172908474901327 | 0.1655634314253885 |
| 0.2499868551321523 | 0.9171844613455501 | 0.1655231211985129 |
| 0.7499203100214695 | 0.4172687478871174 | 0.1654387667046757 |
| 0.7499892667149802 | 0.9172227708241284 | 0.1655186501412538 |
| -0.0006262718467909 | 0.1676278232811492 | 0.1673763654493681 |
| 0.0000218462260773 | 0.6673052677706756 | 0.1651389950611404 |
| 0.5002080150254743 | 0.4923829066090966 | 0.2397020006401266 |
| 0.5000671409580478 | 0.9911281176350205 | 0.2403734270983170 |
| 0.2499503889445422 | 0.2425485704161711 | 0.2414595468638217 |
| 0.2503715635799276 | 0.7420091753186316 | 0.2394718856841261 |
| 0.7497437657781073 | 0.2427353965274799 | 0.2412877211511769 |
| 0.7498753660521260 | 0.7423190087306437 | 0.2386202910335801 |
| 0.4971183521991265 | 0.5103344425680865 | 0.7572064977008131 |
| 0.2501073305954317 | 0.2509571152698502 | 0.7648628855978875 |
| 0.2393950156921670 | 0.7356643752304098 | 0.7628934046784511 |

| | | |
|---|---|---|
| 0.7503075664582023 | 0.2452959602860674 | 0.7656014488774808 |
| 0.7650129346331505 | 0.7615611275830924 | 0.7516478745897539 |
| 0.2502061506964477 | 0.0711255685547612 | 0.5750924931344177 |
| 0.2498246820314810 | 0.5753749444203696 | 0.5717083375336445 |
| 0.7487625233691546 | 0.0629250630665516 | 0.5827112769611974 |
| 0.7504482758712585 | 0.5722282224728369 | 0.5727294593087440 |
| 0.4999837830879173 | 0.3222409130986358 | 0.5771054866744745 |
| 0.5128425729924815 | 0.8268781144907090 | 0.5812498471196820 |
| 0.0003064841485796 | 0.3220176814586702 | 0.5771739479510940 |
| -0.0136033224452881 | 0.8271607113569275 | 0.5775598230434753 |
| 0.2488999749612032 | 0.0922187162805560 | 0.0943937170973044 |
| 0.2498157228223644 | 0.5923135352777869 | 0.0917312712261407 |
| 0.7495364072679970 | 0.0929519137995091 | 0.0940176054508942 |
| 0.7499693400161834 | 0.5922922488565920 | 0.0911687739833439 |
| 0.4994383015828607 | 0.3429834030606436 | 0.0920271352896744 |
| 0.4999610645871243 | 0.8427426515477076 | 0.0905879896004075 |
| 0.4902511156347402 | 0.1688587526847350 | 0.9144634486024081 |
| 0.4990459954691839 | 0.6525701500317350 | 0.9063329937307335 |
| -0.0001408337987722 | 0.1579515629543390 | 0.9067031081999548 |
| -0.0000929420790513 | 0.6570552238314723 | 0.9057734269313452 |
| 0.2484294925347887 | 0.4266553130480402 | 0.8998498975859639 |
| 0.2383870766331370 | 0.9199312002694683 | 0.9059900477638059 |

| | | |
|---|---|---|
| 0.7505431285061108 | 0.4119310884851553 | 0.9035263110291116 |
| 0.7674646623492439 | 0.9243843450154872 | 0.9049124268248333 |
| 0.5011427046456526 | 0.1725417060673094 | 0.4295664844734467 |
| 0.5086628455769894 | 0.6722159312142494 | 0.4241456392871973 |
| -0.0014868317453195 | 0.1724705504745637 | 0.4297775971848256 |
| -0.0077737599079729 | 0.6717979449278830 | 0.4232575505792410 |
| 0.2501981577468892 | 0.4219791506757293 | 0.4265619866651781 |
| 0.2505582442364971 | 0.9220493195426231 | 0.4274356720702061 |
| 0.7498490362292231 | 0.4184283510481810 | 0.4274338383752441 |
| 0.7498187982159952 | 0.9253817354250005 | 0.4277919057753811 |
| 0.0005252070315049 | 0.3420501878495912 | 0.0912471774789913 |
| -0.0000039438130576 | 0.8421638180605585 | 0.0918968750629798 |
| -0.0002796000186234 | 0.4918112711351757 | 0.2394297602021266 |
| -0.0000020020058419 | 0.9910390738296302 | 0.2408438923043828 |
| 0.5094772008427746 | 0.0119259660562514 | 0.7574051486132060 |
| -0.0012574040498368 | 0.5076290403250576 | 0.7582778203839091 |
| 0.0026358766042474 | -0.0038497573839062 | 0.7479999768175616 |

SCAN-relaxed Li-Ni antisite cell 2–POSCAR

| | | |
|---|---|---|
| 1.00000000000000 | | |
| 5.5966022035565208 | 0.0000000000000000 | 0.0000000000000000 |
| 0.0000000000000000 | 10.3403040580396208 | 0.0000000000000000 |
| 0.0000000000000000 | -0.6272774369044152 | 14.2424985948558618 |
| Li | Ni | O |
| 24 | 24 | 48 |
| Direct | | |
| 0.5070362497011653 | 0.0095446130388616 | -0.0000431808235738 |
| 0.4963472566614918 | 0.5122031754453470 | -0.0053426808864315 |
| 0.0042989758461165 | 0.9978269395224312 | 0.0048726214806071 |
| -0.0081140898834236 | 0.5077198046203106 | -0.0031288430595525 |
| 0.2507546619145678 | 0.2431947312328591 | -0.0005467499130879 |
| 0.2505136944506259 | 0.7547226812201380 | 0.0037732033599859 |
| 0.7518266749930450 | 0.2459494426491057 | 0.0009728661332403 |
| 0.7517384668995566 | 0.7565979004540557 | 0.0074472535722681 |
| 0.2504696242678366 | 0.0793564387122576 | 0.3296480090819562 |
| 0.2501503760318408 | 0.5908009356427343 | 0.3335385405149141 |
| 0.7524743410512152 | 0.0772679749350472 | 0.3258188689844865 |
| 0.7521799649848963 | 0.5881703164615714 | 0.3319128421878441 |
| 0.4962413917101333 | 0.3210524270074062 | 0.3388626059018021 |

| | | |
|---|---|---|
| 0.5072211890602144 | 0.8239128417244012 | 0.3336044134985036 |
| -0.0078954680109084 | 0.3246802759113351 | 0.3368371046885981 |
| 0.0044871550222754 | 0.8361022680068969 | 0.3282447765601116 |
| 0.4974730096451732 | 0.1680272107926838 | 0.6692733197133840 |
| 0.4976125288937543 | 0.6635042538393700 | 0.6640339877414767 |
| 0.2494281438061606 | 0.4158707227710616 | 0.6666735379758096 |
| 0.2496837721881646 | 0.9158877981865653 | 0.6666595771567951 |
| 0.7491884767597667 | 0.4158882053854811 | 0.6666861101987899 |
| 0.7544507867193487 | 0.9177917618542631 | 0.1666540950323700 |
| 0.0010343654004913 | 0.1680717250618058 | 0.6692197760475623 |
| 0.0012295961975496 | 0.6634963441474360 | 0.6640915012334599 |
| 0.4994394723120281 | -0.0026291860730039 | 0.4980805846924869 |
| 0.5000478865111712 | 0.4979422034711555 | 0.4982044064752126 |
| 0.0001897425089382 | -0.0026946792330665 | 0.4980356098044195 |
| -0.0003217949568438 | 0.4978892095011758 | 0.4981600316466190 |
| 0.2484573306901612 | 0.2468877396331286 | 0.5021668631355927 |
| 0.2499815368536051 | 0.7473604725055515 | 0.4979256413537483 |
| 0.7486211087999088 | 0.2472771015085632 | 0.5020817942763631 |
| 0.7504592242695888 | 0.7466279570714931 | 0.4977254443373620 |
| 0.2500094615013299 | 0.0840078863118520 | 0.8353888428736865 |
| 0.2492056945386817 | 0.5845956456169146 | 0.8313035990535472 |
| 0.7505253720391087 | 0.0847949262627520 | 0.8356493300054501 |

| | | |
|---|---|---|
| 0.7494298985925767 | 0.5842550857235193 | 0.8313708655251087 |
| 0.5001270193012902 | 0.3334113079471497 | 0.8351422335723475 |
| 0.4995170305705123 | 0.8339881782011632 | 0.8352548549897829 |
| -0.0002634629178946 | 0.3334614292065872 | 0.8351866312544407 |
| 0.0003101833464507 | 0.8340603200592982 | 0.8353448224479476 |
| 0.5002919242077210 | 0.1663478383590464 | 0.1689964095917508 |
| 0.5001559035229781 | 0.6690029270514541 | 0.1646833189245188 |
| 0.2486794110330031 | 0.4183589215409722 | 0.1666316757816720 |
| 0.2541269893835382 | 0.9181594506225332 | 0.1665526741375686 |
| 0.7483323628608828 | 0.4183211034152837 | 0.1666610500502531 |
| 0.7499298352056640 | 0.9156372729348706 | 0.6666660347490235 |
| -0.0004066094774328 | 0.1653513681862306 | 0.1690891347222260 |
| -0.0003946379690278 | 0.6714979495086564 | 0.1639527650849565 |
| 0.4980661349530579 | 0.5086077912609458 | 0.2323204959191145 |
| 0.4908672231611587 | 0.0151902939164959 | 0.2359415268077459 |
| 0.2475471554812128 | 0.2427784038051385 | 0.2411593168965892 |
| 0.2701944762203641 | 0.7456838952310834 | 0.2450328912286745 |
| 0.7315362196363449 | 0.2480871811177895 | 0.2470936388415043 |
| 0.7505601550001331 | 0.7355496234771968 | 0.2387007411234068 |
| 0.4994320927962019 | 0.5094314026270734 | 0.7576465833637919 |
| 0.2498208500651805 | 0.2572305045842597 | 0.7617414078235965 |
| 0.2493127813796764 | 0.7615470535466883 | 0.7600124928230424 |

| | | |
|---|---|---|
| 0.7502890259736250 | 0.2589973324770475 | 0.7606951605086927 |
| 0.7498792072835070 | 0.7635929183229719 | 0.7565345675690847 |
| 0.2490646038493072 | 0.0698947425238269 | 0.5733404415779232 |
| 0.2498840388844902 | 0.5741462248626509 | 0.5715670946340465 |
| 0.7495353439599234 | 0.0677194622201886 | 0.5767452976771212 |
| 0.7503007150159604 | 0.5724214369240510 | 0.5726080314756279 |
| 0.4987349599316870 | 0.3221082541115903 | 0.5757308940197858 |
| 0.5123807540439091 | 0.8260363910932611 | 0.5755352808814844 |
| -0.0007793470103601 | 0.3221748261296258 | 0.5755381373999280 |
| -0.0124216131386475 | 0.8262926552852430 | 0.5754887479582581 |
| 0.2702685220795185 | 0.0899984985459260 | 0.0884064865887823 |
| 0.2477967809703560 | 0.5931912294503221 | 0.0921251125950508 |
| 0.7507449719410001 | 0.1004202940258817 | 0.0946664572418548 |
| 0.7308979304327233 | 0.5875317279741400 | 0.0861556654537765 |
| 0.4979986307837710 | 0.3273390671490463 | 0.1012181025353001 |
| 0.4905849922972231 | 0.8202923923243918 | 0.0974147662721923 |
| 0.5108485299105052 | 0.1632444401413213 | 0.9099424739162524 |
| 0.4988574069428643 | 0.6600475311667312 | 0.9039087170051490 |
| -0.0087561153048470 | 0.1627845822837220 | 0.9107012772511103 |
| -0.0017067829334849 | 0.6596111318569000 | 0.9048465443007164 |
| 0.2499222391031792 | 0.4106292358609375 | 0.9081522987062762 |
| 0.2506130134646195 | 0.9113687198102600 | 0.9083203557255817 |

| | | |
|---|---|---|
| 0.7496480595923116 | 0.4123303082120764 | 0.9069868799419835 |
| 0.7498551771620201 | 0.9078877875774146 | 0.9096797462308058 |
| 0.4982182820266876 | 0.1717060701760755 | 0.4293789471501866 |
| 0.5107180588645418 | 0.6684413281883510 | 0.4233071752213460 |
| -0.0023948405827619 | 0.1720232940051717 | 0.4285419433095616 |
| -0.0087371030295758 | 0.6687795969230926 | 0.4227243684994339 |
| 0.2496026780840797 | 0.4208464559367792 | 0.4251927946749203 |
| 0.2505577295048065 | 0.9203918096185836 | 0.4249599482081454 |
| 0.7494338207571671 | 0.4191768101518207 | 0.4263933256984651 |
| 0.7499244826261655 | 0.9237212574496415 | 0.4235593868554158 |
| -0.0020427736671787 | 0.3327583649309173 | 0.0998405394636773 |
| 0.0172040190115826 | 0.8286971953541554 | 0.0948003514049669 |
| -0.0020204272703240 | 0.5044492867021853 | 0.2330987141886564 |
| 0.0173865925315771 | 0.0072878598311696 | 0.2382754886267937 |
| 0.5125314626790103 | 0.0053149600987289 | 0.7577308510172120 |
| -0.0000367978834814 | 0.5093049422525169 | 0.7578661748529114 |
| -0.0125237783744882 | 0.0050653739098707 | 0.7578021083090779 |

# References

# References

(1) Urrego-Ortiz, R.; Builes, S.; Calle-Vallejo, F. Fast Correction of Errors in the DFT-Calculated Energies of Gaseous Nitrogen-Containing Species. *ChemCatChem* **2021**, *13*, 2508–2516.